



Seismic Performance Analysis of Semi-rigid Steel Frame Based on Panel Zone Mechanical Characteristics of the Joint Experiment Study

Shengcan Lu^{1a}, Minrong Wang^a, Xiangxi Han^{1b}, and Tulong Yin^{1c}

^aSchool of Civil Engineering and Architecture, Wuyi University, Jiangmen 529020, China

^bKey Laboratory of Beibu Gulf Offshore Engineering Equipment and Technology, Education Department of Guangxi Zhuang Autonomous Region, Beibu Gulf University, Guangxi 535000, China

^cCollege of Civil Engineering, Guangdong Communication Polytechnic, Guangzhou 510641, China

ARTICLE HISTORY

Received 24 July 2023
Accepted 12 December 2023
Published Online 15 February 2024

KEYWORDS

End-plate connection
Ductility
Panel zone
Hysteresis characteristics
Failure mode

ABSTRACT

The panel zone, as an important part of the semi-rigid connection (SRC), can effectively affect the force transfer mechanism of the connection. This study aims to evaluate the panel zone mechanical characteristics through test on end-plate connection (EPC) and T-stub connection (TSC) under cyclic loading. Based on failure criteria, the mechanical properties of the panel zone are discussed, including the shear force, plastic energy dissipation, and failure modes. In light of the test studies, an effective and accurate numerical method in OpenSees platform for SRC with a behavior monitored by nonlinear rational springs is proposed. A 4×6 plane steel frame with SRC under the loading stimulation of 12 ground motions is conducted to testify the reliability of the model and analyze the panel zone behavior on the frame. The panel zones exhibit stable hysteresis characteristics and excellent ductility, and the analysis results of the effect of stiffness ratio between bolted connections and panel zone on frame energy consumption provide suggestions for structural energy dissipation design. The model conducts an accurate prediction of semi-rigid connection steel frames (SRCs) seismic behaviors considering the panel zone mechanical properties, and it can dramatically improve computing efficiency and is conducive to seismic design.

1. Introduction

Widely and unanticipated damages in the welded connection of the beam-column in steel frame structures were investigated in earthquake disasters in recent decades (Krawinkler, 1998; Miller, 1998; Whittaker et al., 1998; Chi et al., 2000). Several studies (FEMA-355D, 2000) have indicated that the damage pattern of joints includes brittle fracture of the weld between column and beam, as shown in Fig. 1. Investigators have replaced the conventional 'rigid joint' with the bolted connection to prevent damage at the beam-column joint zone and increase the seismic resistant behavior and maintainability of the frame system. Consequently, the frame system using bolted connection can remove most of types of damage under the earthquake load. Bolted connection steel frame exhibits good ductility. Owing to the nonlinear behavior of the bolted connection and slippage between the bolts and members contact face, the steel frames

system connected with bolts display superior energy dissipation ability in an earthquake, thus removing the risk of fracture damage of the welded members. Moreover, the recommend steel frame structure reduce the cost of assembly and built on-site, consequently, decreasing the quantity of adept labors and making sure dependable building level. Hence, the significant superiority of the bolted connection frame system enables to substitute for the general steel frame with 'rigid joint' in high earthquake area.

A large number researchers have performed the initial experimental study and mechanical research on the earthquake resistant behavior of bolted connections (ANSI/AISC 360-10, 2010; Abidelah et al., 2012; Aydın et al., 2015; ANSI/AISC 341-16, 2016; ANSI/AISC 358-16, 2016; D'Aniello et al., 2017; Gil et al., 2018; Tartaglia et al., 2018; Tartaglia and D'Aniello, 2020; Lu et al., 2021, 2022). Chen performed on semi-rigid connection tests and mechanism analysis, and established the corresponding database (Chen, 2011). On the basis of the seismic characteristics

CORRESPONDENCE Xiangxi Han ✉ 384787419@qq.com 📧 Key Laboratory of Beibu Gulf Offshore Engineering Equipment and Technology, Education Department of Guangxi Zhuang Autonomous Region, Beibu Gulf University, Guangxi 535000, China

© 2024 Korean Society of Civil Engineers

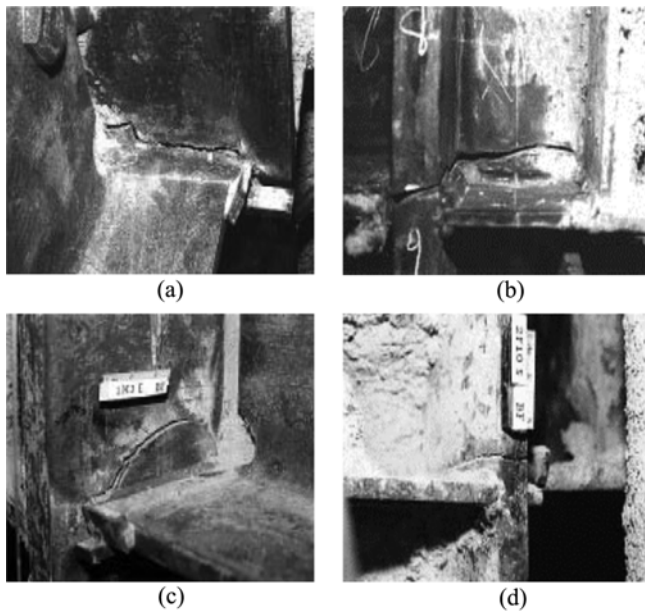


Fig. 1. Welded Joint Failure Mode (FEMA-355D, 2000): (a) Fracture Occurred at Panel Zone, (b) Fracture Developed to the Column Web, (c) Fractures Developed to Column Flange, (d) Fracture Progresses into Column Web

and damaging behavior of bolted connection pattern, the relationship model curves between force and deformation are suggested, providing a reliable theoretical basis for semi-rigid steel frame analysis. Using the computational algorithm of the stiffened end-plate connection, Murray and Sumner (Murray, 2003) introduced an EPC (End-plate connection) analysis method regarding the multiple loads through experiments and theoretical analysis. This work supply a research foundation for ANSI/AISC 358-16 (2016). The European Seismic Standards (Eurocode 3, 2005) took the lead in proposing the concept of the component method which considered the joint as a combination of various members to evaluate the rotational characteristics of the bolted connections. Springs were applied to evaluate the mechanical characteristic of the connection members, and the rotational behavior of the connection was analyzed according to the relationship between various springs. Based on the rotational performance of semi rigid joint, Various scholars (Bayat and Seyed, 2017; Vijay et al., 2020; Rigi et al., 2021; Elhout, 2022) designed multiple high-rise semi-rigid steel frames and rigid steel structures for performance analysis by comparing and analyzing the advantages of rigid joint and semi rigid joint. They discussed the influent of connection rotation stiffness on the seismic performance of steel frame structures. The results showed that semi-rigid frames have a higher probability of complete operational performance under earthquake action. The semi-rigid frame has lower base shear force and higher structural deformation, but the story drift ratio remains within the allowable range and has higher energy absorption capacity. The rotational stiffness of semi rigid joint can have an impact on the performance of steel frames, which cannot be ignored in the design and construction of steel frames.

However, the panel zone is also an important part of the beam-to-column joint. Under the action of the earthquake, the panel zone becomes the weak part, and the horizontal displacement caused by the shear deformation in the multi-story steel frame structure is quite large. Therefore, whether or not the panel zone is enabled to enter the stage of yielding and energy dissipation has become a topic of constant debate in the academic community. The most representative ones are the American Seismic Code Standard and the European Seismic Code Standard. The European standard emphasizes the design philosophy of “strong columns-weak beams”. The American standard points out that the panel zone is allowed to participate in structural consumption under the conditions of stability and strength. The panel zone has good ductility and is a stable shear energy dissipating component. However, excessive shear nonlinear distortion in the panel zone may cause local distortion at the beam-to-column flange of the connection, which increases the possibility of weld fracture at the connection. Therefore, in the actual frame design, the panel zone will have the following three force mechanisms.

Firstly, the panel zone always remains in the elastic stage under the action of the earthquake, and all plastic regions just appear at the beam ends, which meets the design criterion of strong panel zone-weak beam ends. Secondly, all inelastic deformations occur in the panel zone, which is the significant energy dissipation component of the whole structure. The third design concept is a compromise between the above two methods, i.e., both the panel zone and beam ends are involved in the seismic energy dissipation of the whole structure. Nevertheless, accurately predicting the shear strength and stability performance of the panel zone, avoiding the shear buckling instability of the panel zone, and understanding the failure mechanism and energy dissipation capacity of the panel zone are highly important regardless of whether or not panel zone yield is allowed by the assumed design method.

Therefore, many researchers (Kim and Engelhardt, 2002; Brandonisio et al., 2012; Nasrabadi et al., 2013) have proposed different calculation models based on the assumption of pure shear deformation in the panel zone and used them to evaluate the behavior of the beam-to-column connection. However, most of their research focused on the ‘rigid joint’ connection of the center column, ignoring the influence of bolted end-plate members of the joint on the panel zone deformation. Meanwhile, the dynamic behavior of the steel structure system during an earthquake is very complicated, and the bare joint test cannot accurately simulate the actual force characteristics of the frame structure. Therefore, how the behavior of the panel zone is reflected in the overall semi-rigid frame is also important for structural analysis. Considering the shortcomings of previous research on the panel zone of SRC, the present study conducted quasi-static cyclic loading tests on four commonly used semi-rigid connection types, including interior and exterior joints with end-plates connected and interior and exterior joints with T-stubs connected. On the basis of the behavior of the steel frame system considering the distortion of panel zone (as shown in Fig. 2), time history

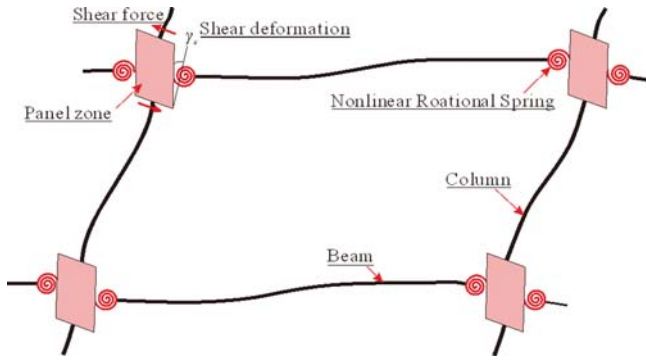


Fig. 2. Steel Frame Calculation Model Considering Panel Zone Deformation

analysis and verification were performed. This study could serve as a reference for the seismic performance design of SRCSFs.

2. Panel Zone Mechanical Properties of SRC

2.1 Shear Strength

Under the horizontal earthquake load, the bending moment (M), axial force (N) and shear force (V) acts on the EPC joint members, including beams, column and panel zone. The relationship between these forces causes complex deformation and stress states in the EPC panel zone, which makes analyzing the mechanical properties of the panel zone more complicated. The forces distribution of the EPC panel zone as an example is displayed in Fig. 3. Assuming the inflection point is at the midpoint of the intersection of the beam and column, the shear force at the panel zone can be calculated by the bending moment at the middle thickness of the beam flange. According to the equilibrium relation of the moment, axial pressure and shear force of the joint panel zone, the equivalent relation of Eq. (1) can be obtained.

$$\left(\frac{M_{b1}}{h_b} + \frac{N_{b1}}{2}\right) + \left(\frac{M_{b2}}{h_b} + \frac{N_{b2}}{2}\right) - V_{c1} - V_{pz} = 0 \quad (1)$$

where M_{b1} and M_{b2} are the bending moment values at the left and right beam ends, respectively; N_{b1} and N_{b2} are the axial force

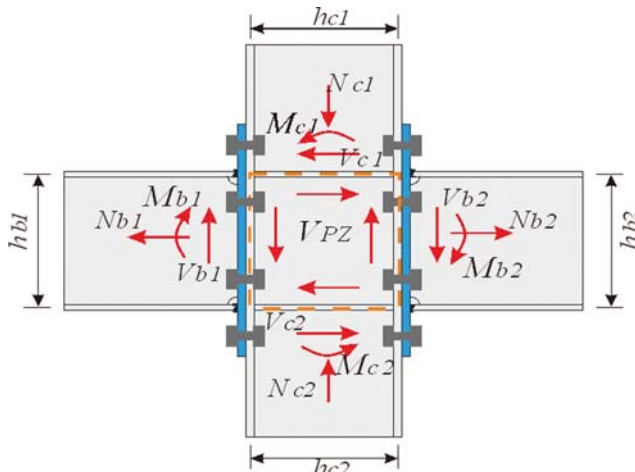


Fig. 3. Force Distribution of Panel Zone

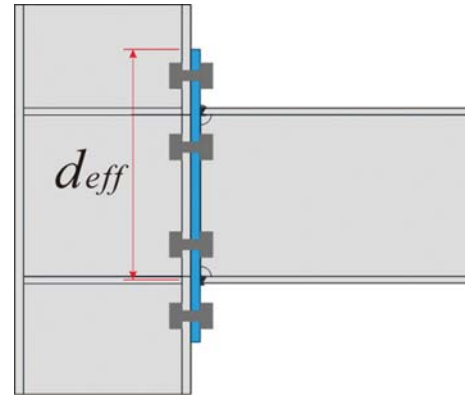


Fig. 4. The Effective Depth of Semi-Rigid Panel Zone

values at the left and right beam ends, respectively. V_{c1} and V_{c2} are the column shear forces above and below the panel zone, respectively. h_{b1} and h_{b2} are the distances of the left and right beam flanges, respectively; h_{c1} and h_{c2} are the distance of the top and bottom column flanges, respectively. The relationship based on the balance of force distribution of the panel zone is calculated using Eq. (2).

$$N_{b1} - N_{b2} + V_{c1} - V_{c2} = 0 \quad (2)$$

Then, the shear characteristic of the panel zone is calculated using Eq. (3).

$$V_{pz} = \frac{M_{b1}}{h_{b1}} + \frac{M_{b2}}{h_{b2}} - \frac{V_{c1} + V_{c2}}{2} \quad (3)$$

From the rotation balance condition of the joint ($M_{c1} + M_{c2} = M_{b1} + M_{b2}$), the average shear strength value of the column section is calculated using Eq. (4) (Brandonisio et al., 2012).

$$V_c = \frac{V_{c1} + V_{c2}}{2} = \frac{M_{c1} + M_{c2}}{H - d_b} = \frac{M_{b1} + M_{b2}}{H - d_b}, \quad (4)$$

where $h_t = (h_{b1} + h_{b2})/2$; $\kappa = h_t/(H - d_b)$, H is the calculated height of the column and d_b is the beam height. Thus, the shear strength value of the panel zone is obtained by using Eq. (5)

$$V_{pz} = \frac{M_{b1} + M_{b2}}{h_t} \cdot (1 - \kappa) \quad (5)$$

According to previous research results (FEMA-355D, 2000), when the panel zone yields, the yield sequence is from the center of the panel zone to the surrounding area. With sufficient bearing capacity, the axial force of the column is completely transferred to the flange of the column and the bolted end-plate connection of the semi-rigid joint. Assuming that the uniform shear force acts on the panel zone, the yield shear strength (V_{ypz}) of the panel zone is calculated using Eq. (6) (Krawinkler, 1978).

$$V_{ypz} = 0.55f_y d_{eff} t_{pz}, \quad (6)$$

where f_y is the yield strength of steel, t_{pz} is the thickness of the panel zone, and d_{eff} is the effective depth of the SRC panel zone, as shown in Fig. 4. Based on the American Prequalified Connections

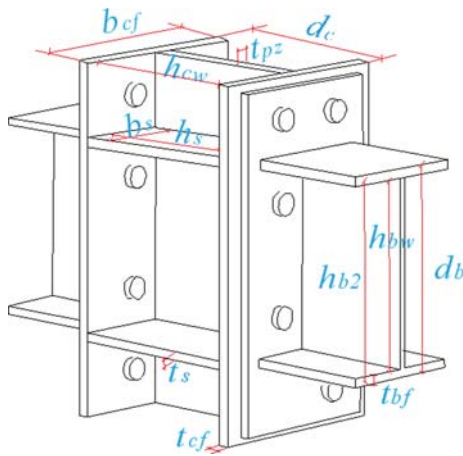


Fig. 5. Design Parameters of the Panel Zone

Code (ANSI/AISC 358-16, 2016), the plastic shear force (V_{ppz}) of the SRC panel zone is determined using Eq. (7).

$$V_{ppz} = 0.6f_y d_c t_{pz} \left[1 + \frac{3b_{cf} t_{cf}^2}{d_b d_c t_{pz}} \right], \quad (7)$$

where b_{cf} is the width of the column flange, t_{cf} is the thickness of the column flange, d_b is the height of the beam section, d_c is the height of the column section and f_y is the yield strength of steel.

2.2 Shear Stability

Based on the requirements of the American Seismic Code (ANSI/AISC 341-16, 2016) and the Chinese Seismic Code (GB/50011-2010, 2010), to reduce the shear buckling distortion of the panel zone, the thickness of the panel zone should satisfy the stability condition as shown in Eq. (8), and the ratio (λ_{pz}) is height to the thickness of the panel zone. The continuity plate characteristic should satisfy the requirements: $t_s \geq t_{bf}$, $h_s = h_c - 2 \cdot t_{cf}$ and $b_s = 0.5 \cdot (b_{cf} - t_{pz})$.

$$\lambda_{pz} = \frac{h_{bw} + h_{cw}}{t_{pz}} \leq 90, \quad (8)$$

where h_{bw} , h_{cw} are the height of the panel zone, continuity plate respectively; t_{bf} , t_s are the thickness of the beam flange, continuity

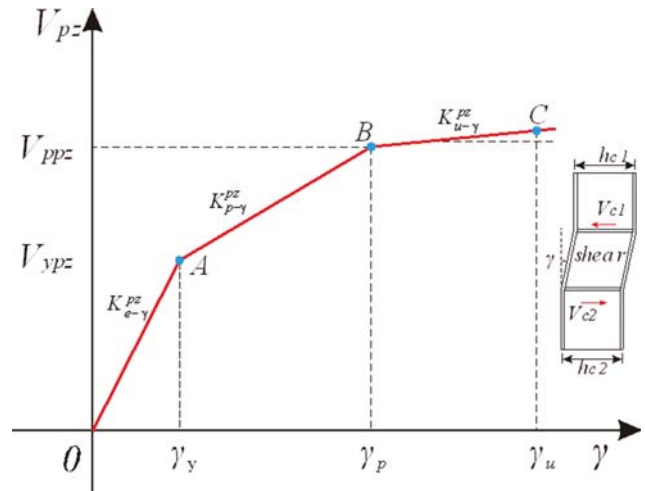


Fig. 6. Shear Constitutive Model of Panel Zone

plate respectively; b_s , is the width of the continuity plate. The corresponding positions of all parameters are shown in Fig. 5.

2.3 The Mechanical Characteristic of the Panel Zone

($V_{pz} - \gamma$)
The mechanical characteristic of the panel zone is a tri-linear curve model, as represented in Fig. 6. The elastic shear deformation stiffness ($K_{e-\gamma}^{pz}$) of the SRC panel zone can be obtained by Eq. (9).

$$K_{e-\gamma}^{pz} = \frac{V_{ypz}}{\gamma_{sy}} = GA_{eff}^{pz}, \quad (9)$$

where γ_{sy} is the yield shear deformation; G is the shear modulus of elasticity and A_{eff}^{pz} is the shear effective area of the panel zone. Krawinkler and Fielding (Krawinkler, 1978) considered that the effective shear area of the panel zone is calculated by using Eq. (10).

$$A_{eff} = (d_c - t_{cf})t_{pz} \quad (10)$$

To discuss the mechanical characteristic of the panel zone after yielding, the elastic-plastic shear stiffness ($K_{p-\gamma}^{pz}$) is expressed by using Eq. (11) (FEMA-355C, 2000; FEMA-355F, 2000).

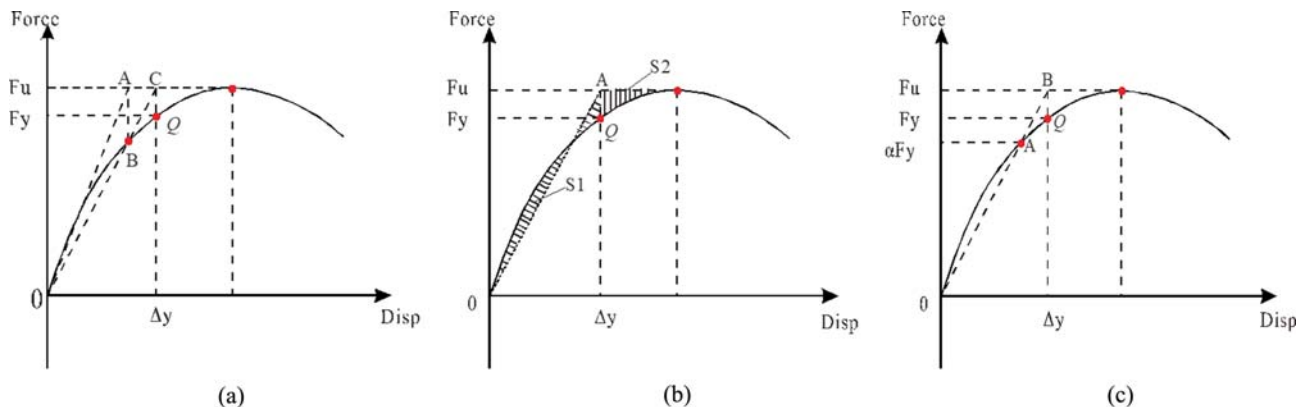


Fig. 7. Performance Division Methods of the Steel Frame. (a) Graphic Method, (b) Area Method, (c) RP Method

$$K_{p-\gamma}^{pz} = \frac{Gb_c t_{ef}^2}{d_{eff}} \tag{11}$$

The ultimate shear deformation stiffness is 2% of the elastic shear stiffness $K_{u-\gamma}^{pz} = 0.02K_{e-\gamma}^{pz}$ and the ultimate shear distortion is six times the elastic shear distortion ($\gamma_{su} = 6\gamma_{sy}$) for the panel zone.

2.4 Failure Criteria

The failure identification methods used in this paper mainly include the graphic method, the area method, and the RP method (Park, 1998; Huang et al., 2011). The mean of the computed results obtained by these approaches is applied to evaluate the yield point of the capacity curves. The ultimate point is determined by the bearing capacity decreasing to 85% of the peak value, and then the structure enters the ultimate stage. The three methods are shown in the Fig. 7. Additional details are provided in References (Lu et al., 2021, 2022) published earlier by the author.

3. Experimental Research Program

3.1 Test Specimens

A six-story semi-rigid steel frame was chosen as the archetype structure, and the details are depicted in Fig. 8. The peak seismic acceleration of the archetype steel frame in Guangzhou, China was 0.1 g with a period of 0.3 5s, and the 50-year probability of exceeding was 10%. The live load (L) and the dead load (D) of each story were 2 and 6 kN/m², respectively. In accordance with the above analysis model and design criteria of the panel zone, two full-scale EPC (exterior and interior EPC) and two full-scale TSC (exterior and interior TSC) were designed for cyclic loading tests. Q345B steel was used in all the members of the specimens, and the beam and column were connected by the end-plate of the bolts with 10.9 M20 friction high-strength bolts (JGJ 82-2011, 2011). The initial and final tightening torques of the bolts were 220 and 446 N·m, respectively, and the diameter of the bolt hole was 22 mm. Specimens EPS, EPM, TSS and TSM correspond to the exterior end-plate connection, interior end-plate connection, exterior T-stub connection and interior T-stub connection. The

beams and columns of the 4 specimens were all hot-rolled I-steel sections, and the beams and columns were 300 mm × 200 mm × 8 mm × 12 mm and 300 mm × 300 mm × 10 mm × 15 mm in size, respectively. The beam length and column height were 1,500 and 3,000 mm, respectively. In accordance with the standard calculation (ANSI/AISC 341-16, 2016), the thickness of continuity plate was 12 mm. An axial pressure of 0.3 was applied at the top of the column. The yield shear force (V_{ypz}), plastic shear force (V_{ppz}), and the stability coefficient of the panel zone (λ_i) were respectively determined using Eqs. (6), (7) and (9). The yield bending moment of beams and columns can be determined by $M_y = W_x \times f_y$, where W_x is the flexural modulus of the section. The plastic bending moment of the beams and columns can be obtained by $M_p = \gamma_x \times M_y$, where γ_x is the plastic development coefficient. The specific connection details are shown in Fig. 9, and the specified details are shown in Table 1 and Table 2. Results show that all specimens meet the stability requirements ($\lambda_i = 38.2 < 90$).

The welding details of the connection were demonstrated in Figs. 9(a) and 9(b). To ensure consistent movement between the beam end and the end-plate, the end plate and the beam end are welded together using complete joint penetration groove welds. The flange and web welds of the beams and columns were all double-sided fillet welds. Stiffeners were welded to both the web and flanges of beam and column using double-sided fillet welds. The loading plates of column end were welded to column with double-sided fillet welds. All welds meet the requirements of the weld specification (GB50661-2011, 2011).

In accordance with steel test sampling and preparation requirements (GB/T2975-2018, 2018), the same batch of test steel (Q345B) was subjected to the tensile test of material properties. Three samples were taken from each test specimen, including those located in the end-plate; T-stub; flange of beam and column; web of beam and column, and bolt. Thus, 21 samples were obtained. The dimension details of the samples and the experimental data are illustrated in Fig. 10 and Table 3, respectively. The test results include the measured thickness and diameter (t/d), yield stress (f_y), limit stress (f_u), elastic modulus (E) and elongation (R). The stress-strain curves of the samples are shown in Fig. 11. The test

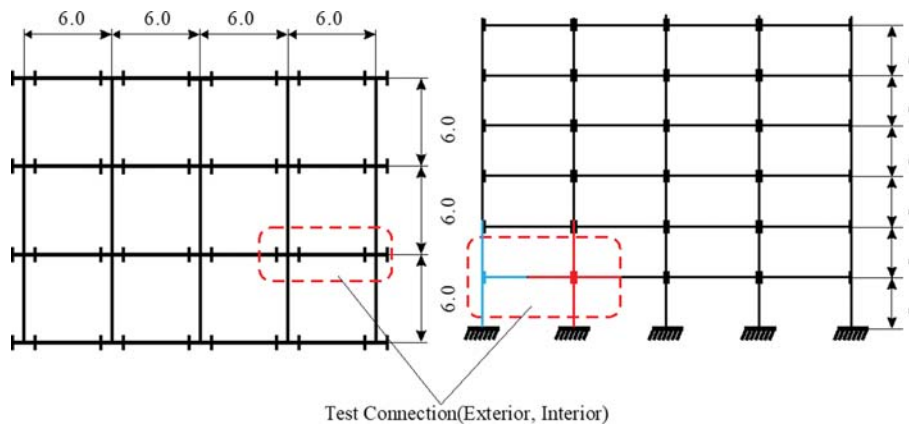


Fig. 8. Prototype Frame Structure and Selected Specimens

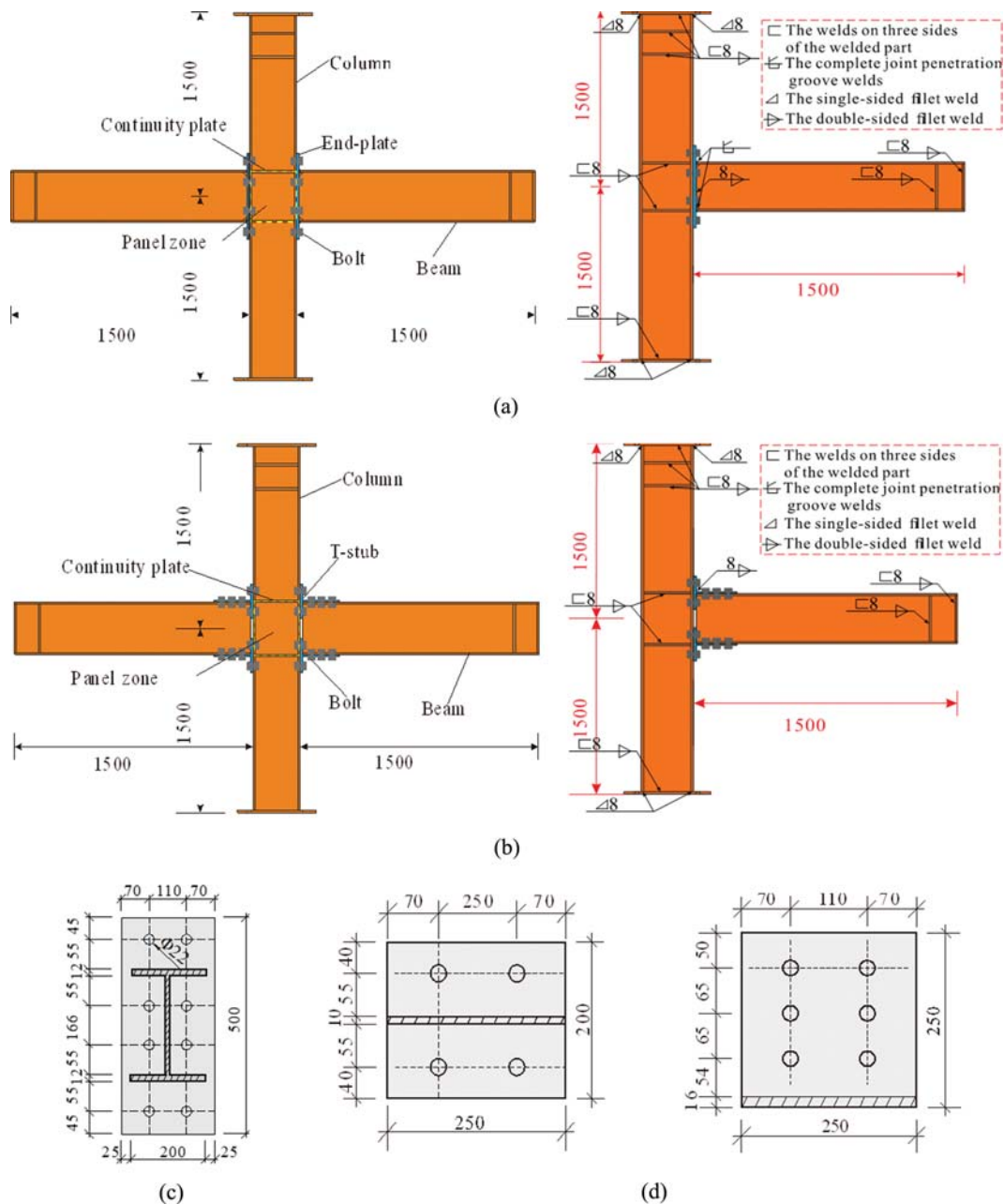


Fig. 9. Test Specimen Details. (a) End-Plate Connection (Interior; Exterior), (b) T-Stub Connection (Interior; Exterior), (c) End-Plate Details, (d) T-Stub Details

results supply the evidence for designing a cyclic loading test equipment and provide material constitutive model for OpenSees calculation of steel frame.

3.2 Test Setup

On the basis of the loading device system of the State Key Laboratory of Subtropical Building Science of the South China University of Technology, the test setup shown in Fig. 12 was designed (the figure is EMP test). The important components of the test device were marked in various colors with numbers 1 – 13 in Fig. 12(a), and the corresponding details of the on-site loading device are shown in Fig. 12(b). The specimen was fixed

on the column hinge support (9) and the beam hinge support (12, 13), and the torsion device (10) was set at the beam end. The MTS actuator (2) with a measuring range of 150 tons (± 250 mm) was installed on the reaction wall (1) by steel bars to exert horizontal low cyclic load on the loading plate at the top of the column.

To exert the vertical axial load at the top of column with constant value and ensure the stability of the test specimens, four ground anchors (8) were connected with the reaction frame (5) of the top column, and the hydraulic jack (6) with the ultimate bearing capacity of 150 tons was fixed by the ground anchor to realise loading with an axial pressure ratio of 0.3 at the top of

Table 1. The Parameters of Each Test Specimen

Specimen	EPS	EPM	TSS	TSM
Connection type				
Column	H300 × 300 × 10 × 15	H300 × 300 × 10 × 15	H300 × 300 × 10 × 15	H300 × 300 × 10 × 15
Beam	H300 × 200 × 8 × 12	H300 × 200 × 8 × 12	H300 × 200 × 8 × 12	H300 × 200 × 8 × 12
End-plate	500 × 250 × 16	500 × 250 × 16		
Continuity plate	270 × 145 × 12	270 × 145 × 12	270 × 145 × 12	270 × 145 × 12
T-stub			500 × 250 × 16	500 × 250 × 16
Bolt	Class 10.9 M20	Class 10.9 M20	Class 10.9 M20	Class 10.9 M20
Axial pressure ratio	0.3	0.3	0.3	0.3
λ_i	38.2	38.2	38.2	38.2

Table 2. The Design Parameters of Members

Member	Section	M_y (kN·m)	M_p (kN·m)	V_{yz} (kN) (Exterior/Interior)	V_{pz} (kN) (Exterior/Interior)
Column	H300 × 300 × 10 × 15	472.650	529.368	—	—
Beam	H300 × 200 × 8 × 12	268.755	301.006	—	—
Panel zone	300 × 300 × 10	—	—	442.408/802.659	536.783/1022.238

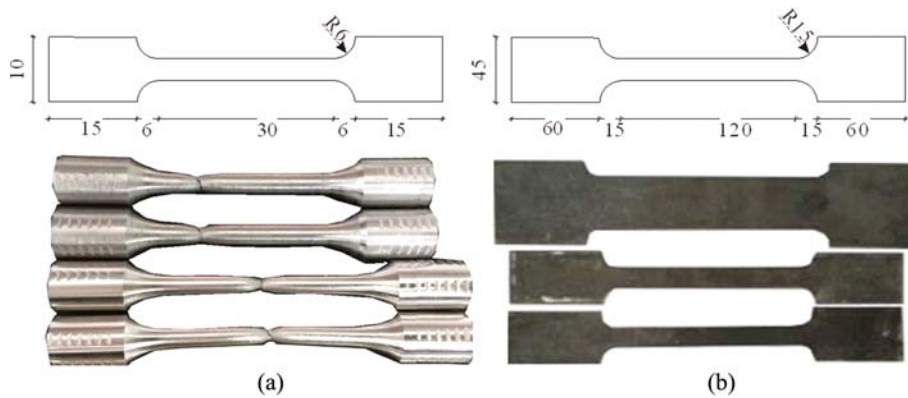


Fig. 10. Tensile Test of Specimens. (a) Bolt Samples, (b) Steel Samples

Table 3. Test Results

Sample	t/d (mm)	f_y (Mpa)	f_u (Mpa)	E (Gpa)	R (%)
Beam flange	12	361	526	185	47.5
Column flange	15	364	550	189	41.1
Beam web	8	382	578	193	31.4
Column web	10	380	548	193	40.0
End-plate	16	379	534	189	31.4
T-stub	16	375	540	191	32.3
T-stub	10	381	541	198	27.6
Bolt	20	998	1165	209	49.8

Note: The data in the table are the average measured values of three samples in each group

column. The axial pressure ratio is $\rho = F_c / (f_c \cdot A_c)$, where f_c is the compressive strength of the steel, taken as 310 MPa according to material properties of Q345B steel and A_c is the cross-sectional area of the column. Therefore, the axial force applied to the top column is $F_c = 110.9$ ton. A spherical hinge rolling device is set between the hydraulic jack and the top column and the value of the hydraulic jack is kept constant through manual intervention. The specific arrangement of the force sensor has been marked in Fig. 12(b), in which No. 1 force sensor records the axial pressure value of the hydraulic jack; The No. 2 force sensor records the force applied by MTS actuator in the horizontal direction of column end; The No. 3 and No. 4 force sensor record the reaction

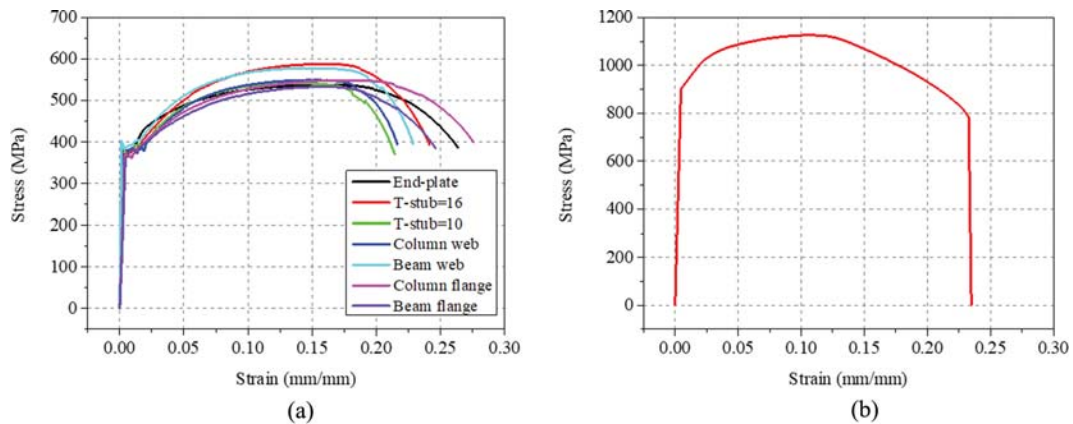


Fig. 11. The Stress-Strain Curve of Samples. (a) Steel Samples Stress-strain Curve, (b) Bolts Stress-Strain Curve

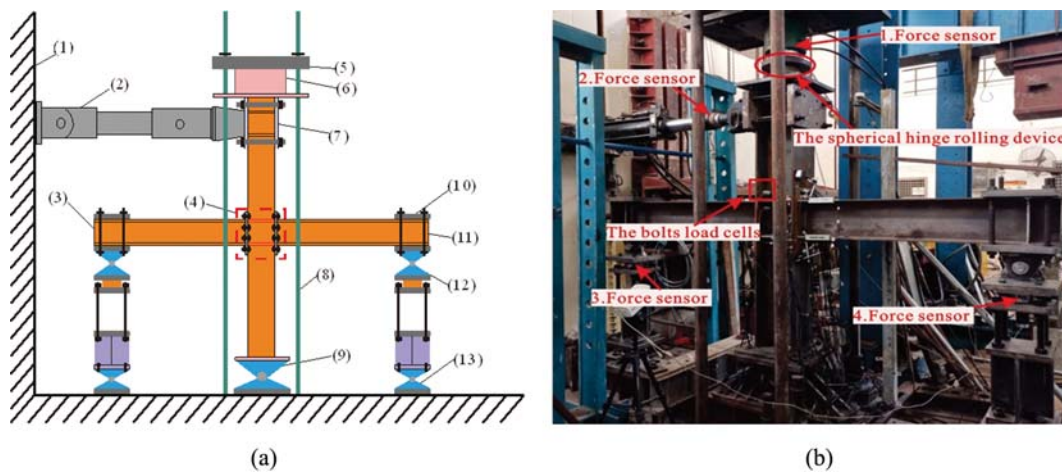


Fig. 12. Test Setup: (a) Test Loading Device Diagram, (1) Reaction Wall; (2) MTS Actuator; (3) Displacement Meter (E3); (4) Connection; (5) Reaction Frame; (6) Hydraulic Jacks; (7) Displacement Meter (P3); (8) Ground Anchor; (9) Column Hinge Support; (10) Torsion Restraint; (11) Displacement Meter (W3); (12) Beam Hinge Support; (13) Beam Hinge Support, (b) On-Site Loading Device Diagram

forces of the left beam end and right beam end during the test, respectively. Displacement meters P3, E3 and W3 were arranged at the top of column (7) and beam ends, respectively. In addition, various force and displacement sensors, gauges and image acquisition instrument were established to monitor the story drift ratio and shear deformation of the panel zone under cyclic load.

3.3 Loading Protocol

The test loading was applied in two steps. Firstly, the axial compression ratio of 0.3 was exerted on top of the column by the jack and remained constant. Secondly, a pseudo-static reciprocating load was exerted at the top of the column by the horizontal displacement control method. The displacement loading system adopts the method recommended by the American Steel Structure Seismic Code (ANSI/AISC 341-16, 2016), as shown in Fig. 13. Six cyclic loadings were applied with top story drift ratios of 0.375%, 0.5% and 0.75%, respectively, and a loading speed of 0.0167%/min. Continuously, four cyclic loadings were applied with a top story drift ratio of 1.0%. Two cycles with top story drift ratios of 1.5%, 2.0% and 3.0% were applied until 8% or the

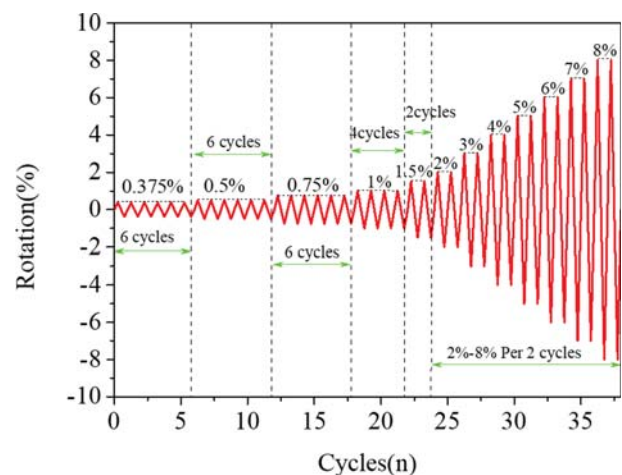


Fig. 13. The Displacement Loading System of the Specimens

test failure, and the loading speed was 0.4%/min. The load was stopped when one of the following conditions was met: 1) the load decreased below 85% of the peak load; 2) the column

buckled; 3) broke obviously and serious buckling deformation occurred in the panel zone.

3.4 Test Measurements

The measurement content of the specimen on the basis of the test model is shown in Fig. 14. The displacement sensors (D1, D2, D3, D4) were arranged along the beam flanges and two linear variable differential transformers (LVDTs; P1, P2) were assigned diagonally at the panel zone to observe the distortion of the end-plate and column flange and the shear distortion of the panel zone. Displacement meters (E3, W3, P3) were also arranged at the left and right ends of the beam and the top of the column to measure their horizontal displacement, as shown in Figs. 14(a) and 14(b). In addition to the above force and displacement measurements, a large number of strain gauges were assigned to observe the stress changes of the joint. Three claw strain gauges (p1, p2, p3) were arranged at the panel zone to monitor the deformation of the panel zone and the beam ends and stiffeners were arranged with strain gauges (b1 – b6; c1, c2). The

arrangement of the measuring points of the other joints was the same as that of the end-plate because only the bolted end-plate connection of the four specimens was different.

The deformation of semi-rigid joints mainly included two parts. One is the deformation of the panel zone caused by shear action, and the other is the deformation of connection caused by rotational action. Herein, the deformation of these two parts is calculated simultaneously, firstly, to verify and analyze the force-deformation relationship curve of the panel zone, and secondly, to calculate the deformation of the connected member in preparation for the next step calculation of the overall frame system. In the test, the deformation of bolted end-plate connection and the shear deformation of the panel zone were measured by the displacement meter, as shown in Fig. 15. The rotation of the left and right ends of the beam caused by the deformation of the bolted end-plate connection was calculated using Eqs. (12) and (13), respectively. The panel zone deformation was obtained by the diagonal LVDTs, as shown in Fig. 15(b). According to the law of cosines, the shear deformation (γ) can be calculated using Eq.

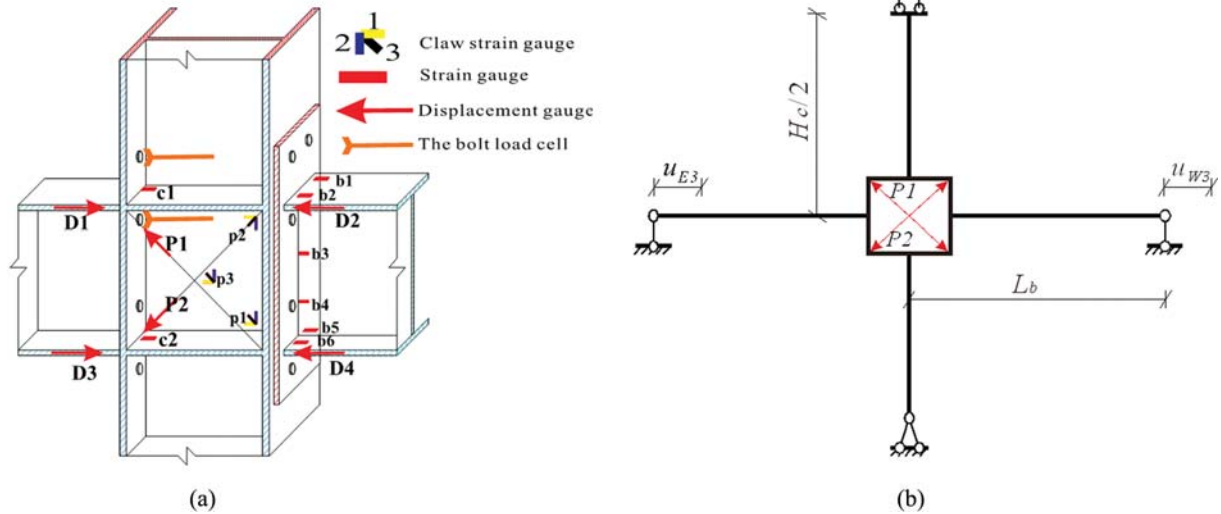


Fig. 14. Measurement Content: (a) Layout of Strain Gauges and Displacement Gauges, (b) Displacement Measurement of Connection

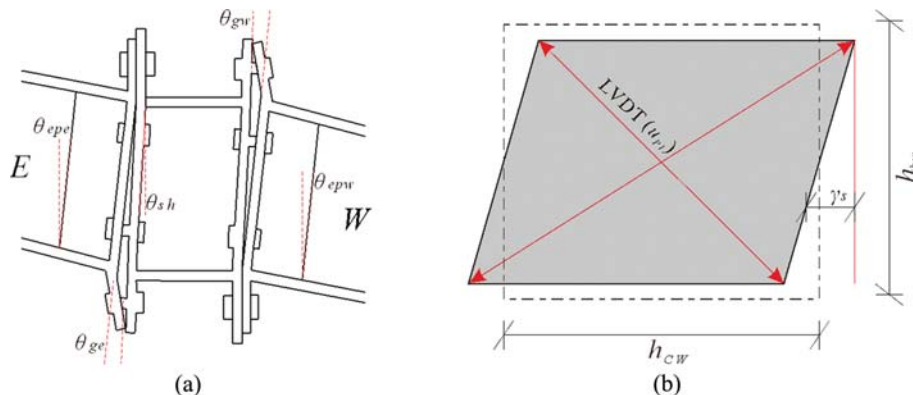


Fig. 15. Schematic Diagram of Joint Deformation Measurement: (a) Bolted End-Plate Connection Deformation, (b) Shear Deformation of the Panel Zone

(14). The value of u_{p3} is the displacement of column top in the horizontal direction; u_{E3} is the horizontal displacement of the right beam end; u_{W3} is the horizontal displacement of the left beam end.

$$\text{Left} \quad \theta_{epe} = \frac{u_{p3} + u_{E3}}{H/2} \quad (12)$$

$$\text{Right} \quad \theta_{epw} = \frac{u_{p3} - u_{W3}}{H/2} \quad (13)$$

$$\gamma_s = \frac{\pi}{2} - \arccos \left[\frac{(h_{bw}^2 + h_{cw}^2) - (\sqrt{h_{bw}^2 + h_{cw}^2} + u_{p3})^2}{2h_{bw}h_{cw}} \right] \quad (14)$$

4. Test Results

4.1 Test Observations and Failure Process

During the cyclic loading test, the failure process of the panel zones mainly includes three stages: elastic stage, elastoplastic stage, ultimate stage. The following sections described the specific failure process.

4.1.1 Specimen EPM

In specimen EPM, the evaluated yielding shear deformation of $\gamma_{sy} = 0.549\%$ was calculated in the primary test stage. The shear force (V_{pz}) of EPM increased linearly with the shear deformation curve until the yield point. At this test stage, the oxide layer was peeled off the panel zone and the yielding state of the end-plate and beam flanges was monitored by the force sensors, which was lead to by the interaction between the bolted end-plate connection. With the beam flanges yielding successively, the panel zone

entered the elastic-plastic stage (Fig. 16(a)). When the specimen EPM entered the elastic-plastic stage until the shear deformation was $4\gamma_{sy}$, the shear force reached the maximum. During this loading process, obvious inelastic shear deformation occurred at the panel zone, which caused the local buckling of the panel zone (Fig. 16(b)). At the last loading phase, the shear force decreased with remarkable deformation owing to the significant buckling of the panel zone, and the test ended because of the fracture at the weld of the end plate (Fig. 16(c)).

4.1.2 Specimen EPS

In specimen EPS, the cyclic load was applied to the EPS to capture the mechanical characteristic of the panel zone and to compare it with the specimen EPM. A calculated yielding shear deformation of $\gamma_{sy} = 0.634\%$ was calculated in the preliminary test stage. Fish-scale lines occurred web of beam and column, which indicated that the bolted end-plate connection yielded (Fig. 17(a)). The hysteresis curves of the panel zone were gradually filled during the $3\gamma_{sy}$ loading, indicating that the panel zone entered the elastic-plastic stage completely. When the shear deformation was approximately $4\gamma_{sy}$, the shear force reached the maximum. Subsequently, black rust of the panel zone flaked off and was accompanied by obvious inelastic shear deformation because of local buckling at the panel zone (Fig. 17(b)). Moreover, the bolts bent differently owing to the compress and tension interaction between the end-plate and the column flange. However, the shear force did not show a downward trend. With the increasing inelastic shear deformation of approximately $6\gamma_{sy}$, the bolt fracture and sliding tooth failure occurred (Fig. 17(c)) and the test stopped.

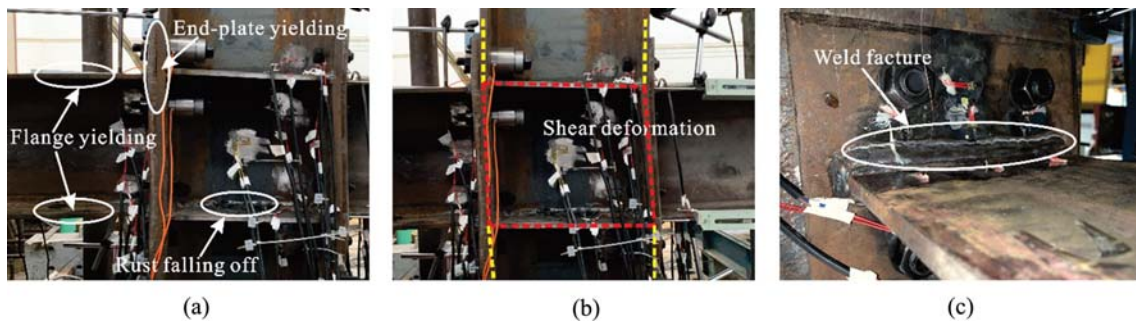


Fig. 16. Specimen EPM Failure Process: (a) Yield Stage, (b) Elastoplastic Stage, (c) Ultimate Stage

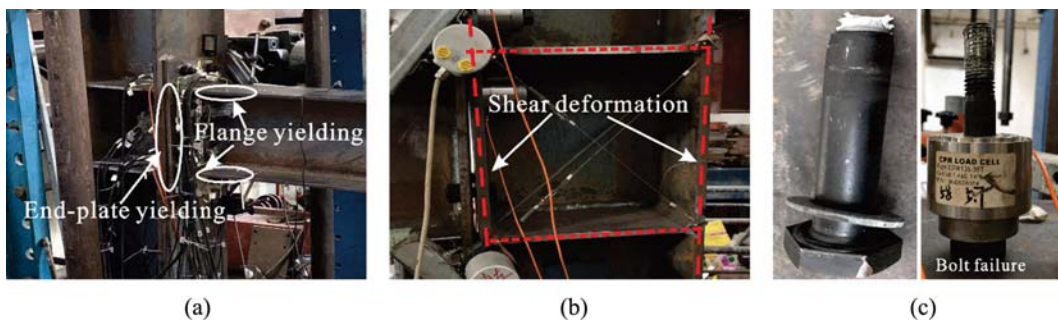


Fig. 17. Specimen EPS Failure Process: (a) Yield Stage, (b) Elastoplastic Stage, (c) Ultimate Stage

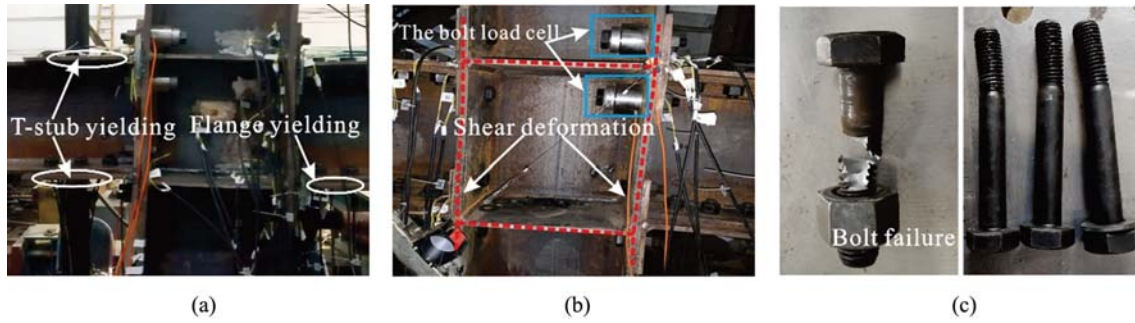


Fig. 18. Specimen TSM Failure Process: (a) Yield Stage, (b) Elastoplastic Stage, (c) Ultimate Stage

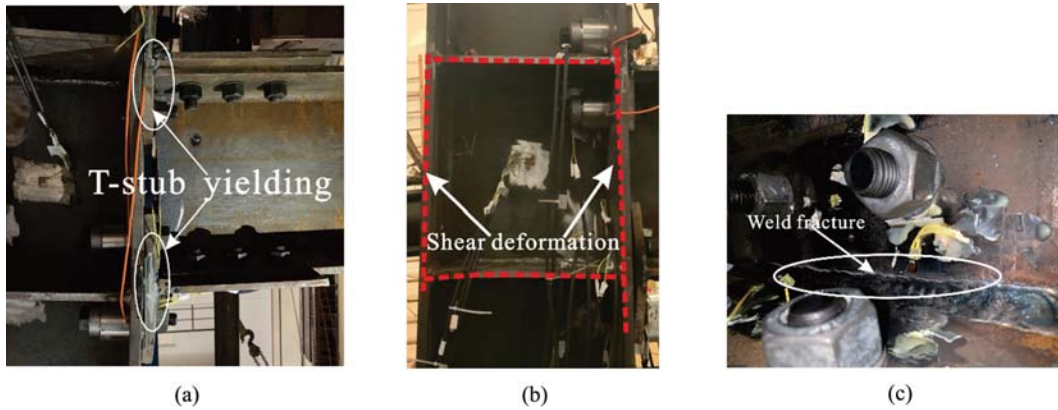


Fig. 19. Specimen TSS Failure Process: (a) Yield Stage, (b) Elastoplastic Stage, (c) Ultimate Stage

4.1.3 Specimen TSM

In specimen TSM, an evaluated yielding shear deformation of $\gamma_{sy} = 0.582\%$ was obtained in the preliminary cyclic test stage. The rust of flanges at beam and column fell off during the $2\gamma_{sy}$ loading process, accompanied by the yielding of the joint (Fig. 18(a)). Afterward, the panel zone showed considerable fish-scale lines and the hysteresis area enclosed by the shear and deformation curve gradually increases, demonstrating that the earthquake energy was credible and effective dissipated by the nonlinear behavior of the panel zone during the cyclic test. At the $4\gamma_{sy}$ test process, an obvious inelastic shear deformation was observed on the panel zone because of the tension and compression interaction between the T-stub and column flanges, accompanied by a slight sliding deformation between the T-stub and bolts (Fig. 18(b)). Meanwhile, the bolts on the left and right sides of the panel zone had different degrees of bending, but the shear force showed no significant decrease. During the $5\gamma_{sy}$ cycle loading, severe local buckling occurred at the panel zone, but the T-stub flanges remained in the initial yielding stage because of the slip effect of bolt holes. Ultimately, the test was stopped because of the excessive distortion of the panel zone and bolt fracture in the final cycle (Fig. 18(c)).

4.1.4 Specimen TSS

In specimen TSS, the cyclic load was applied to the exterior T-stub connection to observe the failure modes and mechanical performance of the specimen. An evaluated yielding shear

deformation of $\gamma_{sy} = 0.622\%$ was calculated in the initial test phase. Fish patterns appeared at panel zone and beam webs, indicating that the connection entered the yielding state (Fig. 19(a)). Subsequently, hysteresis area enclosed by the shear and deformation curves of the panel zone gradually increases during the $2\gamma_{sy}$ loading process accompanied by black rust of the beam flange, and the panel zone peeled off. During the $3\gamma_{sy}$ loading process, the shear force reached the maximum accompanied by the inelastic shear deformation (Fig. 19(b)). With increasing the inelastic deformation of approximately $3.8\gamma_{sy}$, an obvious crack was detected at the weld in the T-stub flange and the test was terminated (Fig. 19(c)). At that moment, obvious buckling behaviors were monitored at the panel zone, but the bolted end-plate connection still remained in the initial yielding state.

4.2 Hysteresis Responses

Figures 20 – 23 show the hysteretic responses of each specimen in the pseudo static loading test, where the shear ratio of panel zone ($V_{pz}/V_{ypz} - \gamma_s$) curves in Figs. 20(a) – 23(a) demonstrate the panel zone hysteretic characteristic, the moment rotation curves ($M - \theta$) in Figs. 20(b) – 23(b) reflect the right connection behavior of the joints and the moment rotation curves ($M - \theta$) in Figs. 20(c) and 22(c) focus on the left connection rotation characteristic of the interior joint. The values of V_{pz} and V_{ypz} were calculated using Eqs. (5) and (6), respectively. The shear deformation γ_s was calculated using Eq. (14), which data were obtained from the LVDT readings. The bending moment (M) is equal to the beam

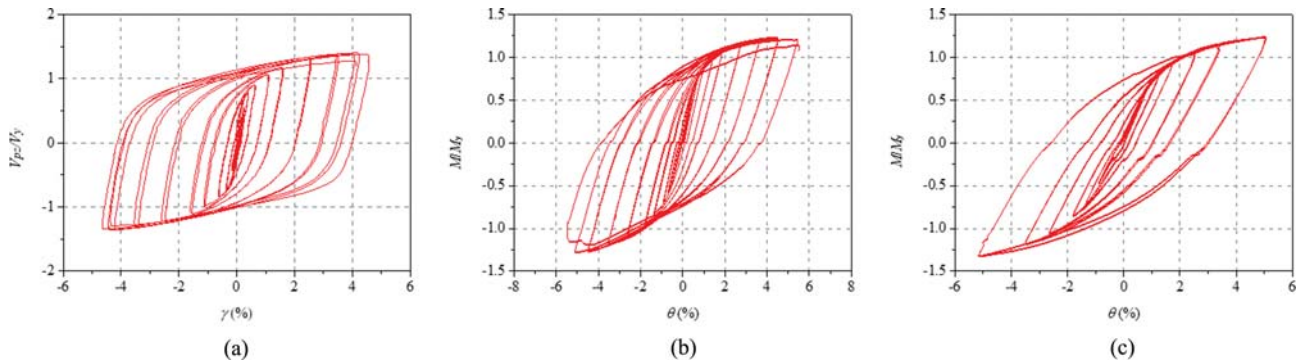


Fig. 20. Hysteresis Curve of Specimen EPM: (a) Shear Ratio of Panel Zone, (b) Right Connection, (c) Left Connection

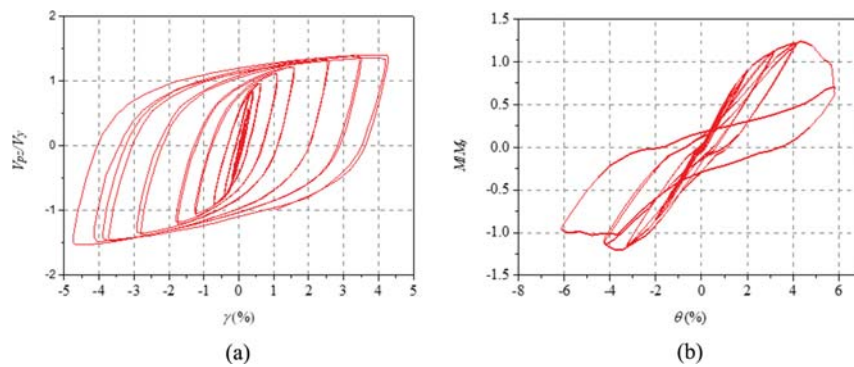


Fig. 21. Hysteresis Curve of Specimen EPS: (a) Shear Ratio of Panel Zone, (b) Right Connection

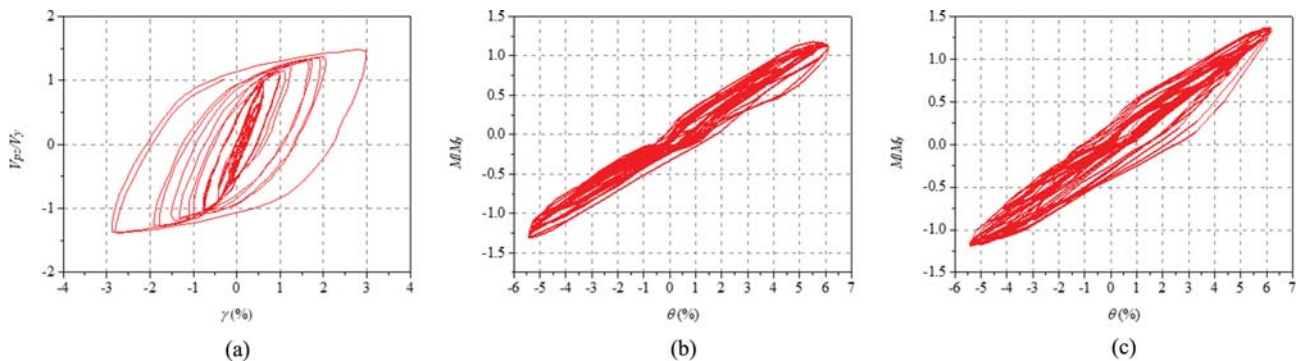


Fig. 22. Hysteresis Curve of Specimen TSM: (a) Shear Ratio of Panel Zone, (b) Right Connection, (c) Left Connection

end reaction force (F) multiplied by the beam length (L), which was obtained by the beam end force sensors. The rotation value (θ) is expressed in Eqs. (12), (13). For the hysteretic responses of curves, all the panel zones showed considerable and stable hysteretic property, illustrating superior seismic behavior in the nonlinear shear distortion with outstanding energy consumption characteristics. No obvious bearing capacity reduction occurred during the cyclic loading test until the post-loading stage. For the moment rotation curves of EPC, the right and left connections of the interior end-plate joint exhibited stable and reliable hysteretic characteristics (Figs. 20(b) and 20(c)). However, the right connection curve showed relatively poor energy consumption characteristics because the sliding tooth failure modes of the bolts occurred at the elastic-plastic loading stage (Fig. 21(b)). The T-stub interior bolted end-plate connection of the joint remained in the initial yielding state (Figs.

22(b) and 22(c)). Thus, the moment rotation curves showed relatively low energy consumption capacity. However, for the exterior bolted end-plate connection, the hysteresis curve showed a relatively large area because more bolted end-plate connections entered the elastic-plastic energy consumption stage (Fig. 23(b)).

4.3 Skeleton Curves

The skeleton curves of the panel zone were extracted from the hysteretic curves, as shown in Fig. 24, where the characteristics of the curve of calculation of the interior connection (CM) and calculation of the exterior connection (CS) were determined from the calculated values from Eqs. (6), (7), (9), and (11). The shear strength of the panel zone increased gradually with the increment of shear distortion, demonstrating that the panel zone performed a reliable mechanical characteristics until the last

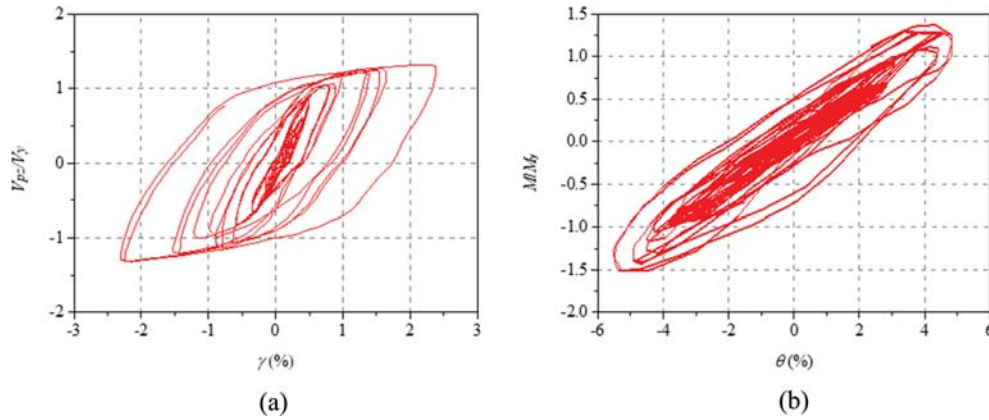


Fig. 23. Hysteresis Curve of Specimen TSS: (a) Shear Ratio of Panel Zone, (b) Right Connection

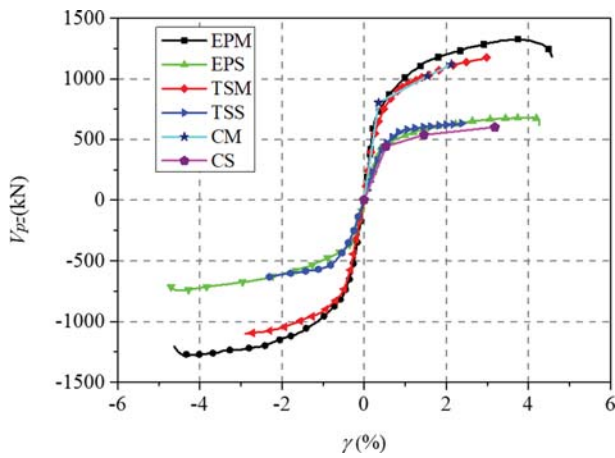


Fig. 24. Skeleton Curve of Specimens Panel Zone

test phase. The curves showed significant hardening behavior, illustrating that the curves obtained from all experiments showed a tri-linear model, which is consistent with the calculated ones. However, the slight difference between the test and calculated values can be ascribed to the fact that the calculated model does not consider the contribution of the bolted end-plate connection to the overall strength. In addition, the EPCs illustrated higher relative strength than the TSCs.

Table 4 shows the value of performance points of the specimens, including the yield, peak and ultimate point and ductility factor,

which were calculated by the skeleton curves based on the failure criteria (Section 2.4). The ductility factor (μ) can be calculated by the ultimate and yield shear deformation as evaluated by $\mu = \gamma_{su}/\gamma_{sy}$. Notably, the panel zone can sustain the maximum shear distortion (γ_s) of the tests from 0.549% to 4.576%, and the average values of yield shear deformation (γ_y) of the EPCs and TSCs were 0.592% and 0.602%, which are approximately 1.2 times $[\gamma_{sy}] = 0.5\%$, respectively. $[\gamma_{sy}]$ is the proposed yield shear deformation of the SRC panel zone (FEMA-355D, 2000). The mean values of the ultimate shear distortion (γ_{su}) of EPCs and TSCs were 3.923% and 2.682%, which are approximately 2 – 4 times $[\gamma_{su}] = 1.0\%$, respectively. $[\gamma_{su}]$ is the proposed ultimate shear distortion of the SRC panel zone (FEMA-355D, 2000). The value of $[\gamma_{sy}]$ and $[\gamma_{su}]$ are shown in the red brackets in Table 3. Meanwhile, the stop conditions of each specimen are also shown in Table 4, including weld fracture, bolt fracture, and the loading stroke limit. It can be seen that even if the end of the skeleton curves in the panel zones are still in the rising stage, as shown in Fig. 24, the whole connections have failed. The ductility coefficient of the specimens was approximately 5.00, indicating that the panel zone exhibited excellent plastic deformation ability and reliable ductility.

4.4 Energy Dissipation Capacity

On the basis of the mechanical property of the panel zone, the energy consumption characteristic is illustrated in Fig. 25. The cumulative energy dissipation ($E_C = \Sigma E_c$) can be calculated by

Table 4. Shear Strength and Ductility Capacities of Specimen Panel Zone

Specimen	Yield point		Peak point		Ultimate point		K_{ypz} (kN/rad)	μ	Stop test conditions
	γ_{sy} (%)	V_{ypz} (kN)	γ_{sp} (%)	V_{ppz} (kN)	γ_{su} (%)	V_{upz} (kN)			
EPM	0.549(0.5)	961.625	3.746	1326.883	4.576(1.0)	1182.915	264680.268	5.78	△
EPS	0.634(0.5)	520.309	4.100	681.386	4.267(1.0)	616.480	117446.705	5.03	☆
TSM	0.582(0.5)	884.004	2.980	1177.555	2.980(1.0)	1177.555	259556.231	5.12	☆
TSS	0.622(0.5)	532.351	2.384	632.608	2.384(1.0)	632.608	116089.956	3.83	◇/○
CM	0.354(0.5)	802.659	1.541	1022.238	2.124(1.0)	1118.586	226807.692	6.00	-
CS	0.531(0.5)	442.408	1.458	536.783	3.186(1.0)	601.166	101040.525	6.00	-

Note: △ represents weld fracture; ☆ represents bolt fracture; ○ represents the load stroke limit; ◇ represents weld crack.

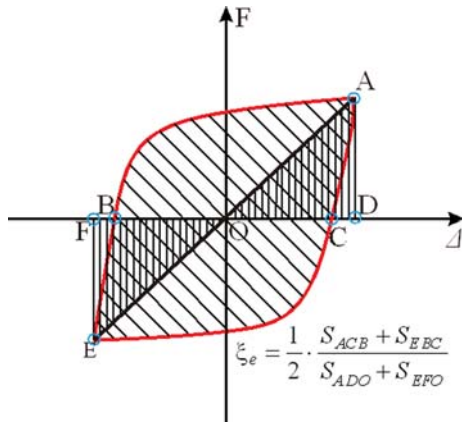


Fig. 25. Energy Dissipation Calculation Diagram

the energy consumption ($E_e = 2\pi\xi_e$) of each cycle loading, where $\xi_e = (S_{ACB} + S_{EBC})/2(S_{ADO} + S_{EFO})$; S_{ACB} , S_{ADO} , S_{EFO} and S_{EBC} are the areas surrounded by curves ACB , ADO , EFO and EBC , respectively.

The cumulative energy dissipation (E_c) of each specimen panel zone at different performance points is shown in Fig. 26. Comparison of the panel zone of different connections showed that those with the EPCs demonstrated better energy dissipation capacity than those with the TSCs. For the EPC panel zone, the cumulative energy consumption increased evidently when the panel zone entered the elastic-plastic stage because of the yielding and inelastic shear deformation of the panel zone.

After the yielding point, the total energy dissipation values of specimen EPM at peak and ultimate points were 807.24 and 1264.83 kN·m/rad, respectively, whereas those of specimen EPS were 438.68 and 515.18 kN·m/rad correspondingly. For specimen TSM, the ultimate point was the same as the yielding point in the skeleton curves. As a result, the total energy dissipation values of the yielding and ultimate points were 78.31 and 322.91 kN·m/rad, respectively, whereas those of TSS were 25.60 and 137.31 kN·m/rad, respectively. For the EPCs panel zone, the ultimate

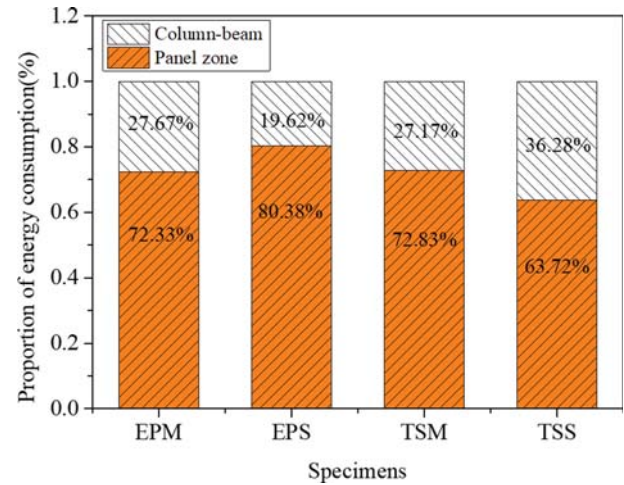
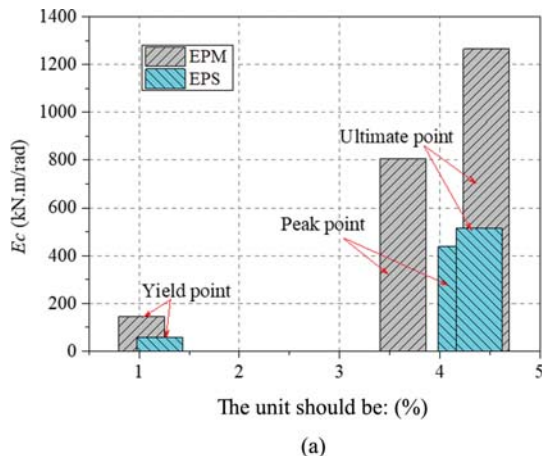


Fig. 27. Energy Consumption Ratio between Components

point of specimen EPM was 36.17% higher than the energy consumption value of the peak point, whereas that of specimen EPS was only 14.85%. For the TSC panel zone, the peak point of specimen TSM was 75.71% higher than the energy consumption value of the yielding point, whereas that of specimen TSS was 81.18%. This result indicated that the different failure modes between specimens can significantly influence the energy dissipation of the panel zone.

The comparison of the energy dissipation components ratio of each connection is shown in Fig. 27. The panel zone can provide very stable and considerable energy consumption, whereas column-to-beam components exhibit relatively low energy consumption capacity. Therefore, within a reasonable design range, the panel zone can effectively improve the energy dissipative capacity of bolted connected steel frame.

5. The Performance of Panel Zone in the Overall Frame

Previous studies only concentrated on the performance of the

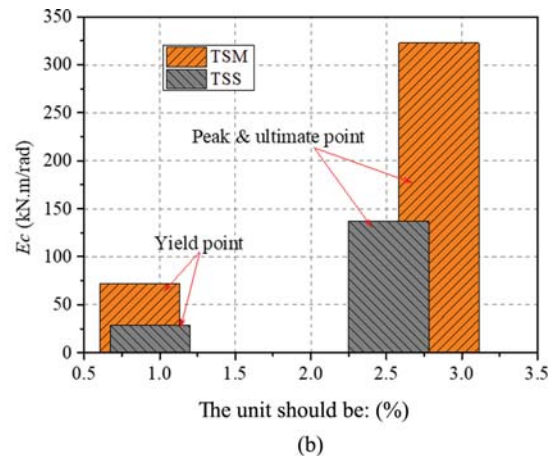


Fig. 26. The Cumulative Energy Consumption of Each Specimen at Different Performance Points: (a) Specimens of EPM and EPS, (b) Specimens of TSM and TSS

panel zone with different types of connections. The performance of the overall frame only by the research on the panel zone level is not sufficient and convincing. Therefore, time history analysis with the prototype frame of the test connection was implemented through the OpenSees software platform to verify the feasibility of the behavior of the SRC panel zone in the frame structure and provide design suggestions. The specific size and load distribution of the prototype structure are described in Section 3.1.

Using OpenSees (OpenSees, 2013) to model the bolted connected steel frame is displayed in Fig. 28. The section of H-shaped steel was simulated by the fiber layer model. The beams and columns were all dispBeamColumn elements, and the steel material property used the steel02 model. The zero-length element was used to simulate the rotation characteristics of the SRCs and the panel zone. The steel01 model was adopted for the moment rotation curve of the bolted end-plate connection of the joint, and a trilinear model was applied to the panel zone of the joint (see

Section 2.3 for details). The specific parameter values of the bolted end-plate connections were extracted from the hysteresis curves (Figs. 20 and 23), as shown in Table 5. The parameter details of the panel zone are shown in Table 4. The frame was set on the ground, taking into account the P-D effect.

5.1 Seismic Parameter Selection and Ground Motions Input

12 ground motions were selected from ground motion library to

Table 5. The Parameters of the Bolted End-Plate Connections

Specimen	Initial rotational stiffness K_{ic} (kN·m/rad)	Yield moment M_y (kN·m)
EPM	9857.913	190.222
EPS	11402.975	218.846
TSM	5368.795	160.669
TSS	7176.994	191.593

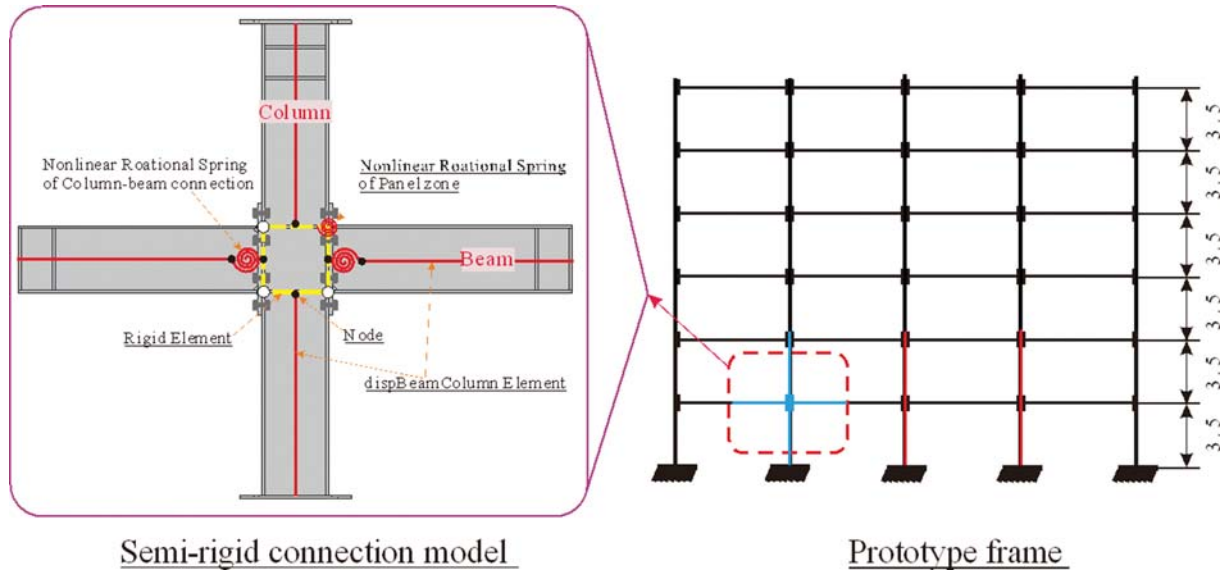


Fig. 28. OpenSees Analytical Model of the Frame

Table 6. The Selected Ground Motion

No.	Earthquake	Date	Station	PGA(g)	Duration (s)	Steps (s)
01	Northridge-01	1/17/1994	Saticoy	0.342	29.99	0.01
02	El Centro	5/19/1940	Array #9	0.211	53.46	0.01
03	Taft	7/21/1952	Lincoln School	0.180	54.37	0.01
04	Kobe	1/16/1995	Abeno	0.231	140	0.01
05	Chi-Chi	9/22/1999	CHY039	0.63	89.995	0.005
06	Lytle Creek	9/12/1970	Cal Edison	0.864	40	0.005
07	Parkfield	6/28/1966	Temblor	0.709	30.42	0.01
08	N. Palm Springs	7/8/1986	Coachella Canal	0.559	59.99	0.005
09	Loma Prieta	10/18/1989	Coyote Lake Dam	0.417	39.99	0.005
10	Duzce Turkey	11/12/1999	Lamont 531	0.124	41.5	0.01
11	Helena Montana-01	10/31/1935	Carroll College	0.477	51.03	0.01
12	Humbolt Bay	2/7/1937	Ferndale City Hall	0.356	40	0.005

use to conduct the time history analysis of the steel frame (PEER, 2005). The specified information of the ground motions is illustrated in Table 6. The seismic peak acceleration (PGAs) of the motions ranged from 0.18 to 0.86 g, which led to various damage level to aboveground structures and can reflect the aboveground structure suffered during the earthquake owing to the wide range of PGAs.

The ground motions were input from the foundation of the structure. Rayleigh damping was used with the ratio of 5%. The whole calculated time of the analytical model is the earthquake duration plus 10 seconds to simulate the free shaking of the whole structure. Thus, the numerical model in Fig. 28 can be used to evaluate the seismic behavior of the frame system accurately.

5.2 Seismic Behavior Evaluation of the Frame

Figure 29 illustrated the relationship between base shear and earthquake motions of the frame with EPCs and TSCs. As presented, the maximum base shear forces of end-plate connected frame were mainly concentrated in No. 05, 07 and 08 ground motions, and its values were greater than 600 kN, whereas only the No. 08 ground motion had a value greater than 600 kN of T-stub connected frame. This difference is mainly due to the lateral stiffness of the frame, indicating that the frame with lower stiffness can significantly reduce the earthquake-induced base shear. The

ground motion peak acceleration values have not obvious influence on the base shear, but increasing lateral stiffness in a certain range can significantly increase the base shear force. Fig. 30 displays the relationship between story drift ratio and ground motions (Figs. 30(a) and 30(b)). As presented, the seismic behavior showed high discreteness owing to the significant difference in period under various ground motions. In end-plate connected frame, all the story drift ratio were not exceed $[\theta_u] = 4\%$, and for the T-stub connected frame (TSC), only No. 05 and 08 ground motions exceeded $[\theta_u] = 4\%$. Where $[\theta_u]$ is the recommended the limit story drift ratio of SRCSFs. Therefore, the whole frame still had a certain strength margin.

Figure 31 shows the distribution of shear deformation along with the height of the panel zone in the frame under different ground motions. As presented, all the maximum shear deformation had no noticeable differences and was less than $[\gamma_{sw}] = 1.0\%$, except No.05 and 08 ground motions. This result illustrates that the panel zone of the frame can supply sufficient strength during the seismic loading and can fully satisfy the design criteria of the structure.

Comparison with the panel zone performance of the test specimens showed that the shear deformation of the whole frame mostly in the range of 0.3 – 0.6% was consistent with the test yield value (Section 4.3). This result indicates that the OpenSees analytical model and the analysis process are reasonable and

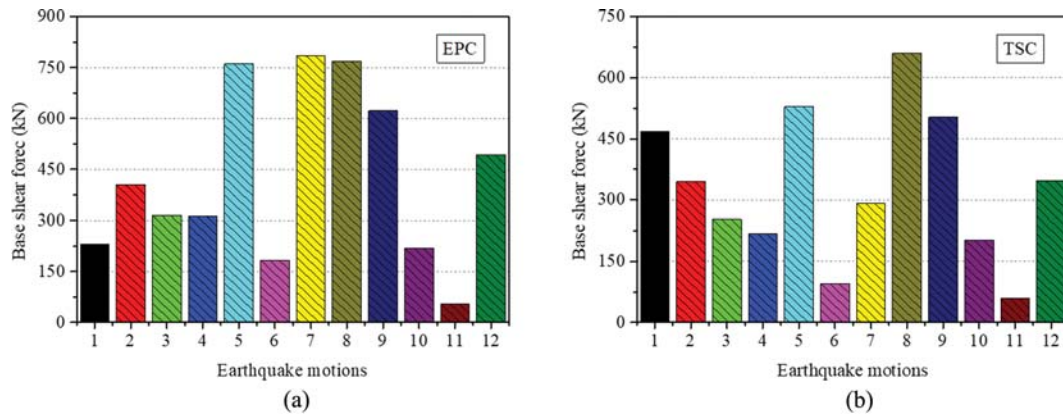


Fig. 29. Maximum Base Shear Force of Frame under Different Earthquakes: (a) End-Plate Connected Frame, (b) T-Stub Connected Frame

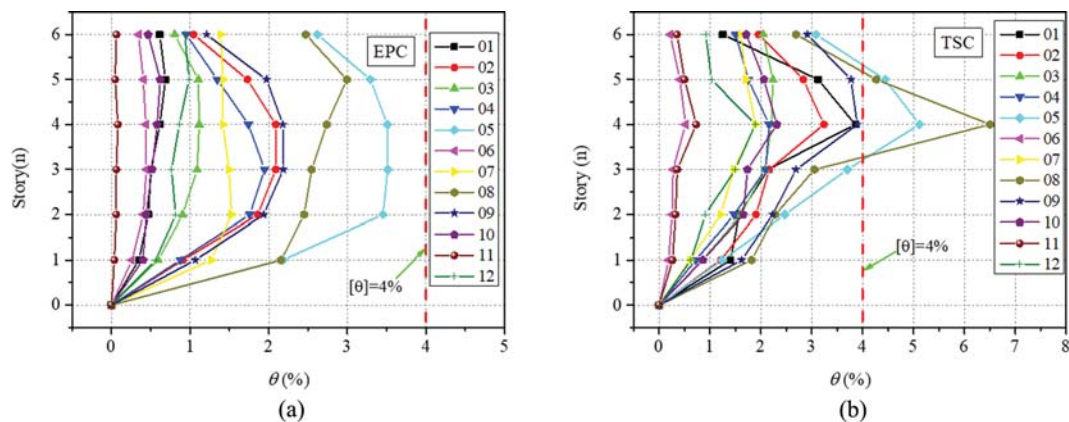


Fig. 30. Maximum Story Drift Ratio of Structures under Different Earthquakes: (a) End-Plate Connected Frame, (b) T-Stub Connected Frame

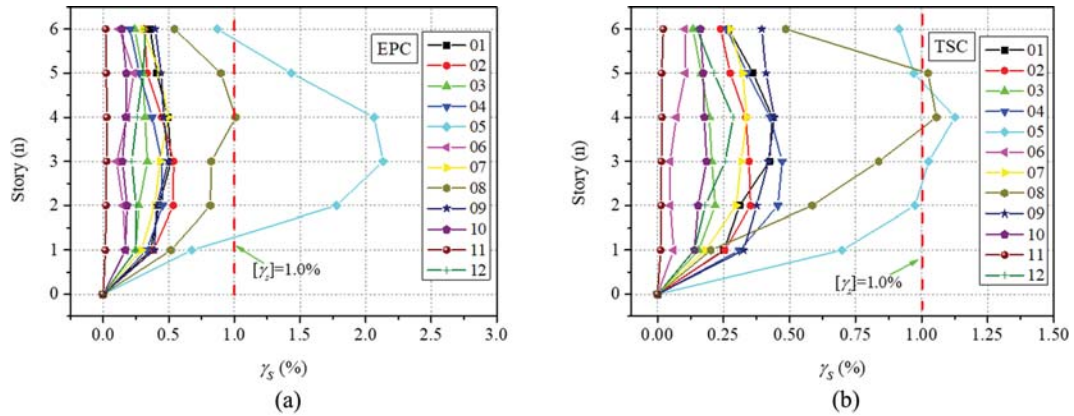


Fig. 31. Maximum Shear Deformations of Frame Panel Zone under Different Earthquakes: (a) End-Plate Connected Frame, (b) T-Stub Connected Frame

accurate. Therefore, the analysis method of SRCsFs considering the performance of the panel zone was proposed in this paper can reliably and effectively reflect the global seismic response of SRCsFs.

5.3 The Effect of Stiffness Ratio (K_{PZ}/K_{CB}) on Frame

Energy Consumption

The initial stiffness ratio (K_{PZ}/K_{CB}) to the panel zone and the bolted end-plate connection is the important factor of the frame energy dissipation. The research (Wang, 2013) shows that the initial stiffness range of commonly used semi-rigid connection is about $1 \times 10^5 \sim 1 \times 10^7$ (kN·m/rad), and based on the above joint

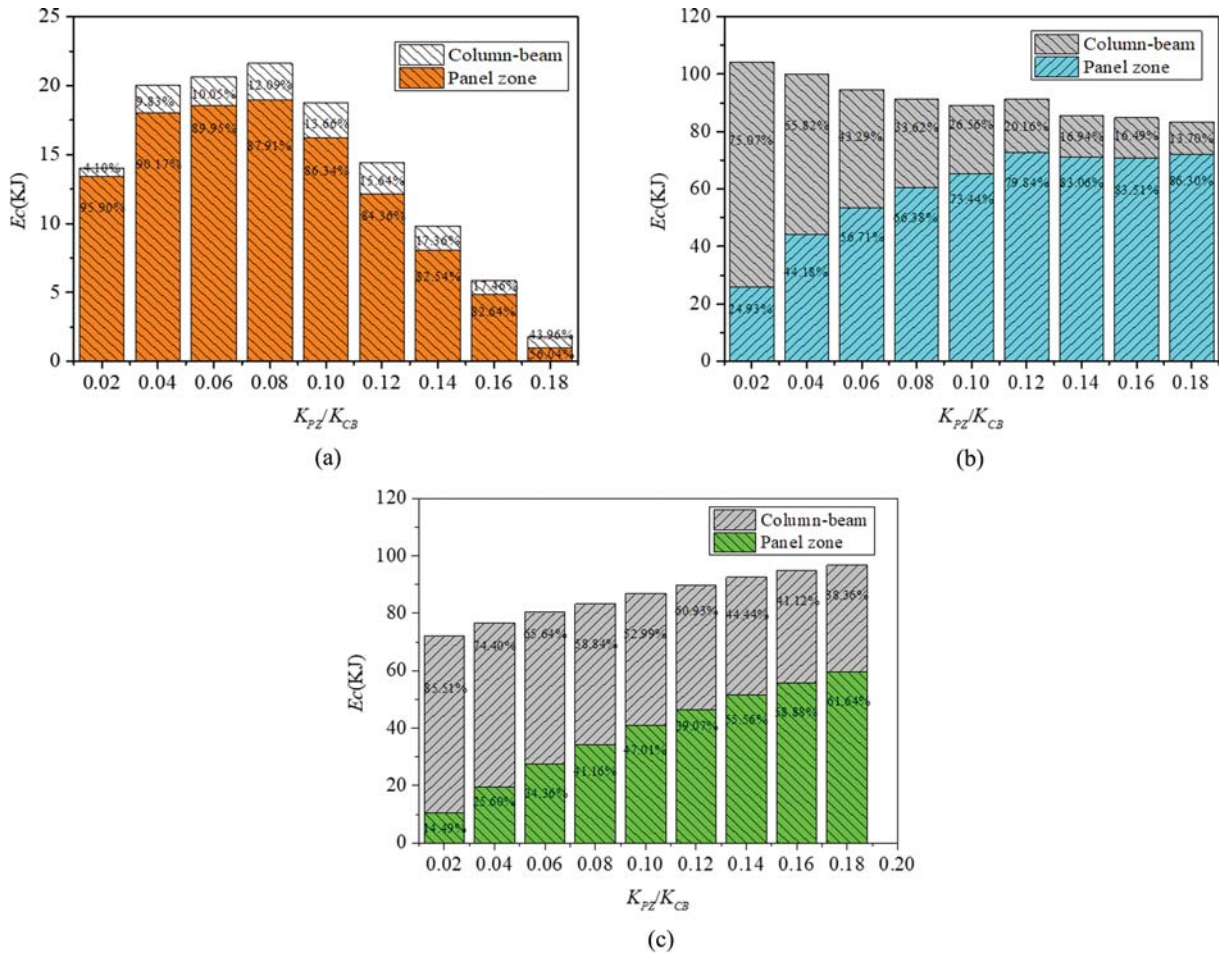


Fig. 32. Cumulative Energy Consumption of Frame with Different Stiffness Ratio (Unit: 1/m): (a) Cumulative Energy Consumption of Frame Corresponding to K_{CB-1} , (b) Cumulative Energy Consumption of Frame Corresponding to K_{CB-2} , (c) Cumulative Energy Consumption of Frame Corresponding to K_{CB-3}

test results in section 4.3, the initial stiffness ratio of the panel zone and bolted end-plate connection range from 0.04 to 0.1(1/m). From the analysis in section 5.2, it can be seen that the peak shear distortion value of the frame is largely distributed in the third and fourth stories of the No. 05, 08 ground motions. Therefore, to better evaluate the energy dissipation of the frame, this part selects the third story of the frame under No. 08 ground motions to analyze the influence of the initial stiffness ratio on energy consumption. The stiffness ratio ranges from 0.02 to 0.2(1/m) in increments of 0.02(1/m) during the simulations.

Figure 32 shows the energy dissipation of the frame with the initial stiffness of bolted end-plate connection ($K_{CB-1} = 1 \times 10^5$ kN·m/rad, $K_{CB-2} = 1 \times 10^6$ kN·m/rad, $K_{CB-3} = 1 \times 10^7$ kN·m/rad). In Fig. 32(a), with the increase of stiffness ratio, the cumulative energy consumption of bolted end-plate connection accounts for the total energy consumption of the frame gradually increasing, but the total energy consumption of the frame shows a trend of increasing first and then decreasing. The total cumulative energy consumption reaches the maximum value within the stiffness ratio range of 0.06 – 0.08. Fig. 32(b) shows the cumulative energy consumption of the frame with the stiffness of the bolted end-plate connection of $K_{CB-2} = 1 \times 10^6$ kN·m/rad. As presented, the maximum value of the cumulative energy consumption occurs in the relatively low stiffness ratio (0.02 – 0.06(1/m)) stage and the bolted end-plate connection account for the main part of the energy consumption, up to 75%. With the increase of stiffness ratio, the cumulative total energy consumption decreases, but the panel zone accounts for the main part of the total energy consumption gradually and reaches the maximum value. After the stiffness ratio is 0.12, the total energy consumption attenuation tends to be stable. Fig. 32(c) demonstrated the total energy dissipation of the frame with the stiffness of the bolted end-plate connection of $K_{CB-3} = 1 \times 10^7$ kN·m/rad. As presented, the total cumulative energy consumption of the frame does not change significantly during the stiffness ratio increases. However, the energy consumption of the panel zone shows a gradual increase trend, and with the stiffness ratio in the range of 0.12 – 0.18(1/m), the energy consumption ratio of the two parts is basically balanced. Therefore, we can select a reasonable stiffness ratio between the bolted end-plate connection and the panel zone according to different connection performance requirements, including whether it is allowed to enter the energy dissipation stage, to effectively enhance the earthquake resistant behavior of the overall structure.

6. Conclusions

A low cyclic loading test is carried out to evaluate the SRC panel zone mechanical property, including EPC and TSC types. On the basis of the test results, an accurate and efficient method of the OpenSees analysis model of the bolted connected panel zone is proposed to capture the SRCF seismic behaviors by nonlinear rational springs. The main conclusions are obtained as follows:

1. The difference between the model calculated bearing

capacity of the panel zone and the experimental results is basically within 10%, illustrating the reasonable and reliability of the proposed tri-linear curve relationship of the panel zone. This shows that the analytical model can accurately simulate the mechanical properties of panel zone, particularly in the elastic and elastic-plastic stages.

2. On the basis of the test results, the SRC panel zone can provide stable and considerable energy consumption, whereas the column-to-beam components illustrate relatively low energy dissipation capacity. Owing to the different failure modes (weld fracture and bolt broken) and processes between specimens, the ultimate point of specimen EPM was 36.17% higher than the energy consumption value of the peak point, whereas that of specimen EPS was only 14.85%. For the TSC panel zone, the peak point of specimen TSM was 75.71% higher than the energy consumption value of the yielding point, whereas that of specimen TSS was 81.18%. The panel zones demonstrate significantly different energy characteristics during the cyclic loading test.
3. In light of the failure criteria, the shear deformation at the yield point of all panel zone specimens ranges from 0.3% to 0.6%, which is correspond to approximately 1.2 times $[\gamma_y] = 0.5\%$. In addition, the ultimate point value of the panel zone ranges from 2% to 4.5%, which are approximately 2 – 4 times $[\gamma_{su}] = 1.0\%$. The panel zones exhibit stable hysteresis characteristics and provide excellent ductility, with the average value is $\mu = 5.00$.
4. According to the stiffness ratio analysis, for the stiffness of the bolted end-plate connection of K_{CB-1} , the total cumulative energy consumption reaches the maximum when the stiffness ratio is in the range of 0.06 – 0.08(1/m). While the maximum value of the cumulative energy consumption occurs at the stage of relatively low stiffness ratio (0.02 – 0.06(1/m)) for the joints with a bolted end-plate connection stiffness of K_{CB-2} . When the bolted end-plate connection stiffness is K_{CB-3} , the stiffness ratio is in the range of 0.12 to 0.18(1/m), and the energy consumption ratio of the two components is basically balanced.
5. Analysis results of SRCF considering the panel zone mechanical property under seismic loads show that the frame meets the requirements of seismic design, and the shear deformation panel zone is approximately consistent with the experimental results. This demonstrated that the calculated process can accurately observe the SRCF seismic behaviors to save computational costs significantly. An accurate analysis model of the panel zone can be obtained by regarding the weak axial direction in further research.

Acknowledgments

This study was sponsored by Launch funding for doctoral research at Wuyi University (Grant No. BSQD2218). The Jiangmen

Basic and Theoretical Science Research Science and Technology Program (Grant No. 92); the National Natural Science Foundation of China (Grant No. 52201304); the Guangxi natural science foundation (Grant No.2019GXNSFAA185044).

Nomenclature

A_c = The cross-sectional area of column
 A_{eff}^{pz} = The shear effective area of the panel zone
 b_{cf} = The width of the column flange
 d_b = The height of the beam section
 d_c = The height of the column section
 d_{eff} = The effective depth of the SRC panel zone
 E = The elastic modulus
 E_c = The cumulative energy dissipation
 E_e = The energy consumption of each cycle loading
 F = The beam end reaction force
 F_c = The axial force of the column
 f_c = The compressive strength of the steel
 f_u = The limit strength of the steel
 f_y = The yield strength of steel
 G = The elastic shear modulus
 H = The calculated height of the column
 h_{b1} = Distance between top and bottom of left beam flanges
 h_{b2} = Distance between top and bottom of right beam flanges
 h_{bw} = The height of the panel zone
 h_{c1} = Distance between top and bottom of left column flanges
 h_{c2} = Distance between top and bottom of right column flanges
 h_s = The height of the continuity plate
 K_{CB} = The initial rational stiffness of connection
 K_{ic} = The initial rotation stiffness of the connection
 K_{ipz} = The initial stiffness of the panel zone
 K_{pZ} = The initial stiffness of panel zone
 $K_{e-\gamma}^{pz}$ = The elastic shear stiffness of the SRC panel zone
 $K_{p-\gamma}^{pz}$ = The elastic-plastic shear stiffness of the SRC panel zone
 $K_{u-\gamma}^{pz}$ = The ultimate shear stiffness of the SRC panel zone
 L = The beam length
 M = The beam section moment
 M_{b1} = The bending moment of left beam
 M_{b2} = The bending moment of right beam
 M_p = The plastic moment of the section
 M_y = The yield moment of the section or connection
 N_{b1} = The axial force of left beam
 N_{b2} = The axial force of right beam
 R = The elongation of the sample
 S_{ACB} = The area of the hysteresis loop ACB
 S_{ADO} = Triangles' area ADO
 S_{AEFO} = Triangles' area EFO
 S_{EBC} = The area of the hysteresis loop EBC
 t_{bf} = The thickness of the beam flange

t_{cf} = The thickness of the column flange
 t_{pz} = The thickness of the panel zone
 t_s = The thickness of the continuity plate
 u = The ductility factor
 u_{E3} = The horizontal displacement of the right beam end.
 u_{P3} = The displacement of the column top in horizontal direction
 u_{W3} = The horizontal displacement of the left beam end.
 V_c = The average shear force of the panel zone
 V_{c1} = The column shear force above the panel zone
 V_{c1} = The column shear force below the panel zone
 V_{ppz} = The plastic shear force of the SRC panel zone
 V_{pz} = The shear force of the panel zone
 V_{ypz} = The yield shear force of the panel zone
 γ_s = The shear deformation the panel zone
 γ_{su} = The ultimate shear deformation
 γ_{sy} = The yield shear deformation
 $[\gamma_{su}]$ = The proposed ultimate shear deformation of SRC panel zone
 $[\gamma_{sy}]$ = The proposed yield shear deformation of SRC panel zone
 λ_{pz} = The stability coefficient of the panel zone
 θ = The rotation of the beam section or the story drift ratio of frame
 $[\theta_u]$ = The proposed ultimate story drift ratio of SRC steel frame
 ρ = The axial pressure ratio the member
 ξ_e = The equivalent damping ratio

ORCID

Shengcan Lu  <http://orcid.org/0000-0001-6491-2779>

Xiangxi Han  <http://orcid.org/0000-0002-1275-9423>

Tulong Yin  <http://orcid.org/0000-0001-8246-1262>

References

- Abidelah A, Bouchaïr A, Kerdal DE (2012) Experimental and analytical behavior of bolted end-plate connections with or without stiffeners. *Journal of Constructional Steel Research* 76:13-27, DOI: [10.1016/j.jcsr.2012.04.004](https://doi.org/10.1016/j.jcsr.2012.04.004)
- ANSI/AISC 341-16 (2016) Seismic provisions for structural steel buildings. Chicago, IL
- ANSI/AISC 358-16 (2016) Prequalified connections for special and intermediate steel moment frames for seismic applications. Chicago, IL
- ANSI/AISC 360-10 (2010) Specification for structural steel buildings. American Institute of Steel Construction, Chicago, Illinois
- Aydın AC, Kilic M, Maali M, Sağroğlu M (2015) Experimental assessment of the semi-rigid connections behavior with angles and stiffeners. *Journal of Constructional Steel Research* 114(4):338-348, DOI: [10.1016/j.jcsr.2015.08.017](https://doi.org/10.1016/j.jcsr.2015.08.017)
- Bayat M, Seyed MZ (2017) Seismic performance of mid-rise steel frames with semi-rigid connections having different moment capacity. *Steel and Composite Structures* 25(1):1-17. DOI: [10.12989/scs.2017.25.1.001](https://doi.org/10.12989/scs.2017.25.1.001)

- Brandonisio G, Luca AD, Mele E (2012) Shear strength of panel zone in beam-to-column connections. *Journal of Constructional Steel Research* 71:129-142, DOI: [10.1016/j.jcsr.2011.11.004](https://doi.org/10.1016/j.jcsr.2011.11.004)
- Chen WF (2011) Semi-rigid connections handbook. USA: J. Ross Publishing
- Chi WM, Deierlein GG, Ingraffea AR (2000) Fracture toughness demands in welded beam-column moment connections. *Journal of Structural Engineering ASCE* 126(2):88-97, DOI: [10.1061/\(ASCE\)0733-445\(2000\)126:1\(88\)](https://doi.org/10.1061/(ASCE)0733-445(2000)126:1(88))
- D'Aniello M, Tartaglia R, Constanzo S, Landolfo R (2017) Seismic design of extended stiffened end-plate joints in the framework of eurocodes. *Journal of Constructional Steel Research* 128(9):512-527, DOI: [10.1016/j.jcsr.2016.09.017](https://doi.org/10.1016/j.jcsr.2016.09.017)
- Elhout E (2022) Location of semi-rigid connections effect on the seismic performance of steel frame structures. *Electronic Journal of Structural Engineering* 22(3):1-10, DOI: [10.56748/ejse.223113](https://doi.org/10.56748/ejse.223113)
- Eurocode 3 (2005) Design of steel structures. Part 1-8: Design of Joints, British Standards Institution, 2005
- FEMA-355C (2000) State of the art report on systems performance of steel moment frames subject to earthquake ground shaking. Washington (DC): Federal Emergency Management Agency
- FEMA-355D (2000) State of the art report on connection performance. Prepared by the SAC Joint Venture for the Federal Emergency Management Agency, Washington D.C.
- FEMA-355F (2000) State of the art report on performance prediction and evaluation of steel moment frame buildings. Washington (DC): Federal Emergency Management Agency
- GB/50011-2010 (2010) Standard for design of steel structure. Ministry of Housing and Urban-Rural Development of the People's Republic of China, Architecture and Building Press, Beijing, China (in Chinese)
- GB/T2975-2018 (2018) Steel and steel products-Location and preparation of samples and test pieces for mechanical testing. PRC, M, Chinese Standard, Standardization Administration Press: Beijing, China (in Chinese)
- GB50661-2011 (2011) The code for welding of steel structures. ministry of housing and urban-rural development of the People's Republic of China. Architecture and Building Press, Beijing, China (in Chinese)
- Gil B, Goñi R, Bayo E (2018) Initial stiffness and strength characterization of minor axis T-stub under out-of-plane bending. *Journal of Constructional Steel Research* 140:208-221, DOI: [10.1016/j.jcsr.2017.10.028](https://doi.org/10.1016/j.jcsr.2017.10.028)
- Huang MS, Liu YH, Sheng DC (2011) Simulation of yielding and stress-strain behavior of Shanghai soft clay. *Computers and Geotechnics* 38:341-353, DOI: [10.1016/j.compgeo.2010.12.005](https://doi.org/10.1016/j.compgeo.2010.12.005)
- JGJ 82-2011 (2011) Technical specification for high strength bolt connections of steel structures. Ministry of Housing and Urban-Rural Development of the People's Republic of China, Architecture and Building Press, Beijing, China (in Chinese)
- Kim KD, Engelhardt MD (2002) Monotonic and cyclic loading models for panel zones in steel moment frames. *Journal of Constructional Steel Research* 58(8):605-635, DOI: [10.1016/S0143-974X\(01\)00079-7](https://doi.org/10.1016/S0143-974X(01)00079-7)
- Krawinkler H (1978) Shear in beam-column joints in seismic design of steel frames. *Engineering Journal AISC* 15:82-91, DOI: [issn/00138029](https://doi.org/issn/00138029)
- Krawinkler H (1998) Earthquake design and performance of steel structures. *Bulletin of the New Zealand Society for Earthquake Engineering* 29(4):285-296, DOI: [10.5459/bnzsee.29.4.229-241](https://doi.org/10.5459/bnzsee.29.4.229-241)
- Lu SC, Wang Z, Pan JR, Wang P (2021) Experimental and numerical research on the multi-stage seismic failure modes of steel frame with end-plate connection. *Structures* 33(10):3495-3514, DOI: [10.1016/j.istruc.2021.06.049](https://doi.org/10.1016/j.istruc.2021.06.049)
- Lu SC, Wang Z, Pan JR, Wang P (2022) The seismic performance analysis of semi-rigid spatial steel frames based on moment-rotation curves of end-plate connection. *Structures* 36(6):1032-1049, DOI: [10.1016/j.istruc.2021.12.064](https://doi.org/10.1016/j.istruc.2021.12.064)
- Miller D (1998) Lessons learned from the Northridge earthquake. *Engineering Structures* 20:249-260, DOI: [10.1016/S0141-0296\(97\)00031-X](https://doi.org/10.1016/S0141-0296(97)00031-X)
- Murray TM, Sumner EA (2003) AISC Steel design guide 4: Extended end-plate moment connections seismic and wind applications. American Institute of Steel Construction, Chicago
- Nasrabadi MM, Torabian S, Mirghaderi SR (2013) Panel zone modeling of flanged cruciform columns: An analytical and numerical approach. *Engineering Structures* 49:491-507, DOI: [10.1016/j.engstruct.2012.11.029](https://doi.org/10.1016/j.engstruct.2012.11.029)
- OpenSees (2013) Open system for earthquake engineering simulation, Version 2.4.2. Berkeley: Pacific Earthquake Engineering Research Center, University of California, <http://opensees.berkeley.edu>
- Park R (1998) State of the art report ductility evaluation from laboratory and analytical testing. Proceedings of Ninth World Conference on Earthquake Engineering, Tokyo, Kyoto, Japan
- PEER (2005) PEER ground motion database. Berkeley, CA: Pacific Earthquake Engineering Research Center, University of California, <http://peer.berkeley.edu/nga>
- Rigi A, Javidsharifi B, Hadianfard HA, Yang T (2021) Study of the seismic behavior of rigid and semi-rigid steel moment-resisting frames. *Journal of Constructional Steel Research* 186(1):106910, DOI: [10.1016/j.jcsr.2021.106910](https://doi.org/10.1016/j.jcsr.2021.106910)
- Tartaglia R, D'Aniello M (2020) Influence of transverse beams on the ultimate behaviour of seismic resistant partial strength beam-to-column joints. *Ingegneria Sismica* 37:50-65
- Tartaglia R, D'Aniello M, Rassati GA, Swanson J, Landolfo R (2018) Full strength extended stiffened end-plate joints: AISC vs recent European design criteria. *Engineering Structures* 159:155-171, DOI: [10.1016/j.engstruct.2017.12.053](https://doi.org/10.1016/j.engstruct.2017.12.053)
- Vijay S, Shrimali MK, Bharti SD, Datta TK (2020) Behavior of semi-rigid steel frames under near-and far-field earthquakes. *Steel and Composite Structures* 34(5):625-641, DOI: [10.12989/scs.2020.34.5.625](https://doi.org/10.12989/scs.2020.34.5.625)
- Wang T (2013) Study on moment-rotation relationship of end-plate connections and seismic behavior of semi-rigid steel frames. Guangzhou: South China University of Technology (in Chinese)
- Whittaker A, Gilani AS, Bertero V (1998) Evaluation of pre-Northridge steel moment-resisting frame joints. *Structural Design of Tall Building* 17:897-912